PHYSICAL REVIEW E **74**, 026705 (2006)

Galilean invariant lattice Boltzmann scheme for natural convection on square and rectangular lattices

R. G. M. van der Sman*
Agrotechnology & Food Sciences, Wageningen University, the Netherlands
(Received 24 September 2005; revised manuscript received 7 June 2006; published 18 August 2006)

In this paper we present lattice Boltzmann (LB) schemes for convection diffusion coupled to fluid flow on two-dimensional rectangular lattices. Via *inverse* Chapman-Enskog analysis of LB schemes including source terms, we show that for consistency with physics it is required that the moments of the equilibrium distributions equal those of the Maxwell-Boltzmann distribution. These constraints can be satisfied for the rectangular D2Q9 lattice for only fluid flow in the *weakly* compressible regime. The analysis of source terms shows that fluxes are really defined on the boundaries of the Wigner-Seitz cells, and not on the lattice sites where the densities are defined—which is quite similar to the staggered grid finite-volume schemes. Our theoretical findings are confirmed by numerical solutions of benchmark problems for convection diffusion and natural convection. The lattice Boltzmann scheme shows remarkably good performance for convection diffusion, showing little to non-numerical diffusion or numerical dispersion, even at high grid Peclet numbers.

DOI: 10.1103/PhysRevE.74.026705 PACS number(s): 47.11.−j, 44.25.+f

I. INTRODUCTION

In a number of previous papers [1–4] we have indicated that further development of the lattice Boltzmann (LB) method can benefit from the study of more simple physical phenomena like (convection) diffusion. Especially we have pointed out the developments with respect to irregular grids or lattices with lower symmetry. In these schemes particles still propagate to adjacent lattice sites, thus without the need for interpolation—like in the traditional lattice Boltzmann schemes.

In this paper we continue this line of research, and present a Galilean invariant LB scheme for natural convection on rectangular grids, in the weakly compressible regime. In natural convection both fluid flow and convection diffusion (of heat) occurs, making it a very suitable problem to stress the parallels between the LB schemes for fluid flow and convection diffusion. We show that the constraints for obtaining a Galilean invariant scheme on rectangular grids are very similar for convection diffusion and fluid flow.

The constraints for constructing LB schemes were first formulated by Koelman [5], and McNamara and Alder [6], implying that the velocity moments of the equilibrium distribution are equal to those of the Maxwell-Boltzmann distribution (which will be denoted as MB constraints in the following). It is observed that all higher order velocity moments of the MB distribution are just in the right form for the Chapman-Enskog expansion of the classical (continuous) Boltzmann equation to deliver the Navier-Stokes Eq. [7]. Thus it is not surprising that also in the discrete case of the lattice Boltzmann equation, the velocity moments should have the same form for consistency with the governing physics, i.e., the Navier-Stokes equation or convection-diffusion equation. Next in consistency with governing physics, the MB constraints guarantee Galilean invariance (up to the order of the MB constraints) and increased stability [7].

For fluid flow the MB constraints have to be satisfied up to *third* order [6], while for (convection) diffusion the MB constraints have to be satisfied one order *lower* [1,2]. Hence exploring the existence of LB schemes on lattices with lower symmetry (like rectangular ones) or even irregular grids is less involving if first investigated for (convection) diffusion, as we have done in previous papers [1,3].

Fluid flow on rectangular grids have been studied previously by Koelman [5] and by Bouzidi and co-workers [8], who stated that the scheme of Koelman is showing anisotropy in viscosity—whereas their own scheme is claimed to be Galilean invariant with isotropic viscosity, albeit with severe stability constraints. The analysis of the scheme has been performed with perturbation analysis of the linearized dispersion equation, which is rarely used to analyze lattice Boltzmann schemes. The analysis of Bouzidi *et al.* is not quite detailed and does not render arguments for instability of the scheme. We will perform the analysis of the LB scheme on rectangular grid with the (*inverse*) Chapman-Enskog expansion, cf. Boghosian and Coveney [9], which does give more insight in consistency, accuracy, and stability.

The *inverse* Chapman-Enskog analysis of convection diffusion and fluid flow will be performed in tandem, in order to stress the highly similarity of the analysis of both phenomena. From a didactical point of view the analysis is also very instructive—as the MB constraints follow naturally from the *inverse* Chapman-Enskog analysis. In particular we emphasize the similarity of (i) analysis of source terms (i.e., volumetric heat dissipation and body forces), and (ii) obtaining schemes of third order accuracy.

The correct formulation of source terms in LB schemes is still an outstanding problem in literature. Most studies [10–12] use a modified equilibrium distribution, and a redefinition of the fluid flow velocity. Below, we conclude that there is no need for this—only one has to realize that the *correct location* of the mass flux (and consequently also the velocity), namely on the boundaries of the Wigner-Seitz cells—is midway on the lattice sites.

By performing (inverse) Chapman-Enskog analysis to third order, we derive conditions for improving the accuracy

*Electronic address: ruud.vandersman@wur.nl

of the LB scheme to third order. As shown below, the Chapman-Enskog analysis is in a way related to von Neumann stability analysis, and consequently the conditions for improved accuracy imply also improved stability.

The validity of our theoretical findings is studied with the numerical analysis of the well-known benchmarks of (i) a Gaussian density profile in a uniform flow field, and (ii) a differentially heated cavity with flow induced by natural convection. Next, a natural convection due to volumetric energy dissipation is investigated which is a problem described by convection diffusion equation with a source term. This last problem is related to novel heating methods of liquid foods like microwave, radio frequency, and Ohmic heating.

II. LB SCHEME

The natural convection problem is solved using two lattice gases with particle distribution functions: $f_i(\mathbf{x},t)$ and $g_i(\mathbf{x},t)$. The density, velocity, and heat energy fields are represented by the hydrodynamic moments of the particle distribution functions:

$$\rho_f(\mathbf{x},t) = \sum_i f_i(\mathbf{x},t),$$

$$\mathbf{j}_f(\mathbf{x},t) = \sum_i \mathbf{c}_i f_i(\mathbf{x},t) = \rho_f \mathbf{u}(\mathbf{x},t),$$

$$\rho_g(\mathbf{x},t) = \sum_i g_i(\mathbf{x},t). \tag{1}$$

The problem is solved on a rectangular D2Q9 lattice, similar to Bouzidi, Lallemand, and Luo [8]. The particle distribution functions evolve following the (generalized) lattice Boltzmann equations with source terms:

$$f_i(\mathbf{x}+\Delta\mathbf{x}_i,t+\Delta t) - f_i(\mathbf{x},t) = -\Omega_{ij}^f[f_j(\mathbf{x},t) - f_j^{eq}(\mathbf{x},t)] + \mathcal{F}_i,$$

$$g_i(\mathbf{x}+\Delta\mathbf{x}_i,t+\Delta t) - g_i(\mathbf{x},t) = -\Omega_{ij}^g[g_j(\mathbf{x},t) - g_j^{eq}(\mathbf{x},t)] + \mathcal{G}_i. \tag{2}$$

These LB equations should render the following balance equations for mass, momentum, and thermal energy:

$$\partial_t \rho_f = -\partial_\alpha j_{f,\alpha},$$

$$\partial_t j_{f,\alpha} = -\partial_\beta \Pi_{\alpha\beta} + F_\alpha,$$

$$\partial_t \rho_g = -\partial_\alpha j_{g,\alpha} + q \tag{3}$$

with fluxes defined as

$$j_{f,\alpha} = \rho_f u_\alpha,$$

$$\Pi_{\alpha\beta} = p\delta_{\alpha\beta} + \rho_f u_\alpha u_\beta - \rho_f \nu(\partial_\alpha u_\beta + \partial_\beta u_\alpha),$$

$$j_{g,\alpha} = \rho_g u_\alpha - D\partial_\alpha \rho_g, \tag{4}$$

Here ν, D are the viscosity and diffusivity, respectively.

The driving force for natural convection is the density differences as induced by temperature gradients, for which the Boussinesq approximation is used, for which holds

$$F_\alpha = \beta \rho_f g_\alpha (\rho_g - \rho_g^0). \tag{5}$$

β is the thermal expansion coefficient of the fluid, g_α is the gravitational acceleration, and ρ_g^0 is the fluid density in the environment. No specific form of the volumetric heat dissipation term q is assumed yet.

We note that under the Boussinesq approximation, the fluid can be taken to be incompressible. The lattice Boltzmann scheme cannot solve incompressible flow, as it is using an ideal gas equation of state. To approximate incompressible flow, the lattice Boltzmann scheme is normally operated in the weakly compressible regime, where pressure differences over the system is small compared to the total pressure. In a sense this quite resembles the Chorin type of schemes.

III. INVERSE CHAPMAN-ENSKOG ANALYSIS

The inverse-Chapman-Enskog analysis [9] is applied to the special case of the lattice BGK scheme, which involves only a single relaxation time—implying $\Omega_{ij} = \omega\delta_{ij}$. In the following the distribution functions will be written in the Dirac notation of bra and ket vectors, $\langle f|$ and $|g\rangle$, having f_i or g_i as components of the column or row vectors. Scalar products are written as a multiplication of a bra with a ket vector: $\langle f|g\rangle$.

In short, the Chapman-Enskog expansion involves (i) Taylor expansion of the left-hand side of the lattice Boltzmann equation, (ii) multitime scale expansion of $|f\rangle$ and the time derivative ∂_t in terms of the Knudsen number ϵ, (iii) collecting terms of equal order of ϵ (rendering a hierarchy of equations), and (iv) taking moments of the hierarchy of expanded equations.

Hence, Taylor expansion up to second order of the left-hand side renders

$$\left(D + \tfrac{1}{2}D^2 + \tfrac{1}{6}D^3\right)|f\rangle = -\omega_f|f^{neq}\rangle \tag{6}$$

with the differential operator D defined as $D = \Delta t(c_{i,\alpha}\partial_\alpha + \partial_t)$. In our notation the operator D is to be viewed as a diagonal matrix.

The multitime scale expansion is based on separation of the time scales of convection and diffusion, denoted as t_1 and t_2. Physical arguments for introducing the multitime scales are rarely given in the lattice Boltzmann literature. We show in Appendix A that the scaling follows naturally from analysis of the LB equation in Fourier space. The multi time scale expansion of the time derivative is then

$$\Delta t\partial_t = \sum_n \epsilon^n \partial_{tn} = \sum_n \epsilon^n S_n. \tag{7}$$

As follows from Appendix A, convection diffusion defines two time scales: t_1 the fast convective time scale, and t_2 the slower diffusive time scale. These time scales are separable in the limit of small density gradients ($\Delta x_\alpha \partial_\alpha \rho/\rho \ll 1$).

Similarly, the spatial derivative in operator D is rewritten as

$$\Delta t\partial_\alpha c_{i,\alpha} = \epsilon C_1 = \epsilon K_\alpha c_{i,\alpha}. \tag{8}$$

Above we have defined the expansion of the time and spatial derivatives. Now, we also apply a multitime scale expansion to the particle distribution function, using $|f^{(0)}\rangle = |f^{eq}\rangle$:

$$|f\rangle = \sum_n \epsilon^n |f^{(n)}\rangle. \tag{9}$$

This is equivalent with wave number expansion of the harmonic perturbation in perturbation analysis.

The source terms are of $\mathcal{O}(\epsilon)$ as they scale with Δt, cf. Buick [11]. We denote $\mathcal{F}\Delta t = \epsilon \mathcal{F}^{(1)}$, $F_\alpha \Delta t = \epsilon F_\alpha^{(1)}$, $\mathcal{G}\Delta t = \epsilon \mathcal{G}^{(1)}$, and $q\Delta t = \epsilon q^{(1)}$.

We substitute the above expansions in the lattice Boltzmann equations, Eq. (2). After collecting terms of equal order in ϵ, we obtain the following hierarchy of equations:

$$\begin{aligned}
|\mathcal{F}^{(1)}\rangle - \omega_f |f^{(1)}\rangle &= D_1 |f^{(0)}\rangle, \\
-\omega_f |f^{(2)}\rangle &= D_1 |f^{(1)}\rangle + \left[S_2 + \tfrac{1}{2} D_1^2\right] \times |f^{(0)}\rangle, \\
-\omega_f |f^{(3)}\rangle &= D_1 |f^{(2)}\rangle + \left[S_2 + \tfrac{1}{2} D_1^2\right] |f^{(1)}\rangle \\
&\quad + \left[S_3 + S_2 D_1 + \tfrac{1}{6} D_1^3\right] |f^{(0)}\rangle.
\end{aligned} \tag{10}$$

It must be noted that in general S_1 and S_2 do not commute, cf. Ref. [13]. However, as will be shown below, in the weakly compressible regime S_2 and S_1 commute. In the above equations, we have already used the commutation of S_1 and S_2. Similarly one obtains the hierarchy of equations $|g^{(n)}\rangle$, and therefore it is not shown.

Governing equations expressed in the collision invariants can be obtained by taking the scalar product of the collision invariant eigenvectors and the hierarchy of equations.

Obtained results will be substituted in equations of subsequent order, and thus involve higher order velocity moments of the equilibrium distributions. Below we have listed the velocity moments up to third order using the Dirac notation:

$$\begin{aligned}
&\langle 1|f^{eq}\rangle = \rho_f; \quad \langle c_\alpha | f^{eq}\rangle = j_{f,\alpha}, \\
&\langle 1|g^{eq}\rangle = \rho_g; \quad \langle c_\alpha | g^{eq}\rangle = j_{g,\alpha}^{(0)}, \\
&\langle c_\alpha c_\beta | f^{eq}\rangle = \Pi_{\alpha\beta}^{(0)}; \quad \langle c_\alpha c_\beta c_\gamma | f^{eq}\rangle = \Gamma_{\alpha\beta\gamma}, \\
&\langle c_\alpha c_\beta | g^{eq}\rangle = Q_{\alpha\beta}; \quad \langle c_\alpha c_\beta c_\gamma | g^{eq}\rangle = R_{\alpha\beta\gamma}.
\end{aligned} \tag{11}$$

$\langle c_\alpha|$ is a row vector with elements being the Cartesian component of the particle velocity $c_{i,\alpha} = \Delta x_i / \Delta t$ propagating in the direction indicated by i. Mind that we have not yet specified the explicit form of the velocity moments, except for the collision invariant moments—as in agreement with the *inverse* Chapman-Enskog analysis [9].

In the following we will frequently use results following from the conservation of mass, momentum, and energy, namely the constraints on the source terms:

$$\langle 1|\mathcal{F}\rangle = 0; \langle c_\alpha|\mathcal{F}\rangle = F_\alpha \Delta t; \langle 1|\mathcal{G}\rangle = q\Delta t \tag{12}$$

and the vanishing moments of the *nonequilibrium* distribution (with $n > 0$):

$$\langle 1|f^{(n)}\rangle = 0; \langle c_\beta|f^{(n)}\rangle = 0; \langle 1|g^{(n)}\rangle = 0. \tag{13}$$

A. First order equations

We proceed to the Chapman-Enskog analysis taking the moments of the hierarchy in Eq. (10). At first order in ϵ we have

$$\begin{aligned}
\langle 1|\mathcal{F}^{(1)}\rangle &= \langle 1|D_1|f^{(0)}\rangle, \\
\langle c_\alpha|\mathcal{F}^{(1)}\rangle &= \langle c_\beta|D_1|f^{(0)}\rangle, \\
\langle 1|\mathcal{G}^{(1)}\rangle &= \langle 1|D_1|g^{(0)}\rangle.
\end{aligned} \tag{14}$$

To analyze the resulting equations, we use that $\langle 1|C_1|f\rangle = K_\beta \langle c_\beta|f\rangle$, $\langle c_\alpha|C_1|f\rangle = K_\beta \langle c_\alpha c_\beta|f\rangle$, and similar $\langle v_n|S_m|f\rangle = S_m \langle v_n|f\rangle$ for arbitrary m, n. Using the above definition of the moments of the equilibrium distributions we obtain

$$\begin{aligned}
S_1 \rho_f + K_\alpha j_{f,\alpha} &= 0, \\
S_1 j_{f,\beta} + K_\alpha \Pi_{\alpha\beta}^{(0)} &= F_\beta^{(1)}, \\
S_1 \rho_g + K_\alpha j_{g,\alpha}^{(0)} &= q^{(1)}.
\end{aligned} \tag{15}$$

Recall that the S_1 operator is the fast time scale derivative ∂_{t1}, and $K_\alpha j_\alpha$ is the divergence of a flux. Hence all above equations have the form of a balance equation (for mass, momentum, and energy, respectively). As the equations are on the fast time scale of convection, they are to be equal to the Euler equations of an inviscid fluid. This implies that the following MB constraints should be satisfied:

$$\begin{aligned}
\langle c_\alpha c_\beta | f^{eq}\rangle &= \Pi_{\alpha\beta}^{(0)} = \rho_f c_s^2 \delta_{\alpha\beta} + \rho_f u_\alpha u_\beta, \\
\langle c_\alpha | g^{eq}\rangle &= j_{g,\alpha}^{(0)} = \rho_g u_\alpha.
\end{aligned} \tag{16}$$

Because the flow field is assumed to be weakly compressible ($K_\alpha u_\alpha \approx 0$), we can replace the convective time-scale operator with a spatial derivative, cf. Flekkoy [14]: $S_1 = -u_\alpha K_\alpha$. Hence

$$D_1 = K_\alpha |c_\alpha - u_\alpha\rangle. \tag{17}$$

Note that the velocity $|\tilde{c}_\alpha\rangle = |c_\alpha - u_\alpha\rangle$ is the peculiar velocity, a quantity often used in kinetic theory.

B. Second order

Taking the moments of the equations in the hierarchy of order ϵ^2 results in the following equations:

$$\begin{aligned}
0 &= \langle 1|D_1|f^{(1)}\rangle + \langle 1|S_2 + \tfrac{1}{2} D_1^2 |f^{(0)}\rangle, \\
0 &= \langle c_\beta|D_1|f^{(1)}\rangle + \langle c_\beta|S_2 + \tfrac{1}{2} D_1^2 |f^{(0)}\rangle, \\
0 &= \langle 1|D_1|g^{(1)}\rangle + \langle 1|S_2 + \tfrac{1}{2} D_1^2 |g^{(0)}\rangle.
\end{aligned} \tag{18}$$

Substitution of $D_1|f^{(0)}\rangle = -\omega_f |f^{(1)}\rangle + |\mathcal{F}\rangle$ and $D_1|g^{(0)}\rangle = -\omega_g |g^{(1)}\rangle + |\mathcal{G}\rangle$ gives

$$S_2\rho_f = -\left(1-\tfrac{1}{2}\omega_f\right)\langle 1|D_1|f^{(1)}\rangle - \tfrac{1}{2}\langle 1|D_1|\mathcal{F}^{(1)}\rangle,$$

$$S_2 j_\beta = -\left(1-\tfrac{1}{2}\omega_f\right)\langle c_\beta|D_1|f^{(1)}\rangle - \tfrac{1}{2}\langle c_\alpha|D_1|\mathcal{F}^{(1)}\rangle,$$

$$S_2\rho_g = -\left(1-\tfrac{1}{2}\omega_g\right)\langle 1|D_1|g^{(1)}\rangle - \tfrac{1}{2}\langle 1|D_1|\mathcal{G}^{(1)}\rangle. \quad (19)$$

Inserting $D_1=\tilde{c}_\alpha K_\alpha$, and using $\langle 1|f^{(n)}\rangle=0$, $\langle c_\alpha|f^{(n)}\rangle=0$, $\langle 1|g^{(n)}\rangle=0$ for $n>0$, renders

$$S_2\rho_f = -\tfrac{1}{2}K_\alpha F_\alpha^{(1)},$$

$$S_2 j_{f,\alpha} = -\tfrac{1}{2}S_1 F_\alpha^{(1)} - K_\beta \Pi_{\alpha\beta}^{(1)},$$

$$S_2\rho_g = -\tfrac{1}{2}S_1 q^{(1)} - K_\alpha j_{g,\alpha}^{(1)}. \quad (20)$$

Having defined the dissipative momentum and heat flux:

$$\Pi_{\alpha\beta}^{(1)} = \left(1-\tfrac{1}{2}\omega_f\right)\langle c_\alpha c_\beta|f^{(1)}\rangle,$$

$$j_{g,\alpha}^{(1)} = \left(1-\tfrac{1}{2}\omega_g\right)\langle c_\alpha|g^{(1)}\rangle. \quad (21)$$

In most previous studies concerning body forces [10–12], the authors have expected $S_2\rho_f=0$ (and $S_2\rho_g=-K_\alpha j_{g,\alpha}^{(1)}$), and consequently use a redefinition for the (convective) flux:

$$\bar{j}_{f,\alpha}^{(0)} = j_{f,\alpha} + \tfrac{1}{2}F_\alpha^{(1)},$$

$$\bar{j}_{g,\alpha}^{(0)} = j_{g,\alpha}^{(0)} + \tfrac{1}{2}q^{(1)}u_\alpha. \quad (22)$$

However, we argue that no *new* definitions of the fluxes need to be introduced, but only the *correct* definitions of the fluxes. As is usually *not* recognized in the lattice Boltzmann literature, the fluxes should really be computed at the interfaces of the Wigner-Seitz cells surrounding the lattice sites [2,15,16]. In Appendix B we show with a simple case problem that the above results are consistent with the correct definition of the flux. Also, no adjudgments of the equilibrium distribution is needed, as suggested in literature [11,12]. Still, the above "redefinitions" are useful approximations of the convective mass and heat fluxes at the center of the Wigner-Seitz cell, from which one also can compute the flow velocity in the center of the lattice cell $\bar{u}_\alpha$.

Also in finite volume schemes [17,18], the fluxes are defined on the boundaries of the control volumes (i.e., lattice cells), and *not* at the cell center. For fluid flow one speaks of staggered grids, where the discretization points of the pressure (i.e., density) field is located at the center of the control volumes, and the discretization points of the velocity field is located midway on the pressure nodes (hence at the boundaries of the control volumes). The velocity field at the centers of the control volumes is obtained via interpolation. Similarly one can interpolate the velocity field in the lattice Boltzmann scheme, cf.

$$j_{f,\alpha}(\mathbf{x},t) = \rho u_\alpha(\mathbf{x},t) = \sum_i c_{i,\alpha}[f_i(\mathbf{x}+\Delta\mathbf{x}_i,t) - f_{i^*}(\mathbf{x},t)] \quad (23)$$

with the index i^* defined by $\mathbf{c}_{i^*}=-\mathbf{c}_i$.

C. Dissipative fluxes

Expressions for the dissipative fluxes are obtained by expressing $|f^{(1)}\rangle$ and $|g^{(1)}\rangle$ in terms of the equilibrium distribution functions, using the first order equations from the hierarchy. Using the definitions of the velocity moments, and $S_1=-u_\alpha K_\alpha$, we obtain the expression for the dissipative heat flux and momentum flux:

$$j_{g,\alpha}^{(1)} = -\left(\tfrac{1}{\omega_g}-\tfrac{1}{2}\right)K_\beta[-u_\beta j_{g,\alpha}^{(0)} + Q_{\alpha\beta}],$$

$$\Pi_{\alpha\beta}^{(1)} = -\left(\tfrac{1}{\omega_f}-\tfrac{1}{2}\right)K_\gamma[-u_\gamma \Pi_{\alpha\beta}^{(0)} + \Gamma_{\alpha\beta\gamma}]. \quad (24)$$

Note that as the source term and the body force should not contribute to the dissipative fluxes, we have demanded that the following moments are zero:

$$\langle c_\alpha c_\beta|\mathcal{F}\rangle = 0; \quad \langle c_\alpha|\mathcal{G}\rangle = 0. \quad (25)$$

To be consistent with convection diffusion and fluid flow, the dissipative fluxes should follow Fourier's and Newton's laws:

$$j_{g,\alpha}^{(1)} = -DK_\alpha\rho_g,$$

$$\Pi_{\alpha\beta}^{(1)} = -\nu(K_\alpha j_{f,\beta} + K_\beta j_{f,\alpha}). \quad (26)$$

These equations are obtained if the following MB constraints are satisfied:

$$Q_{\alpha\beta} = \rho_g c_{s,g}^2\delta_{\alpha\beta} + \rho_g u_\alpha u_\beta,$$

$$\Gamma_{\alpha\beta\gamma} = \rho_f c_{s,f}^2(u_\alpha\delta_{\beta\gamma} + u_\beta\delta_{\alpha\gamma} + u_\gamma\delta_{\alpha\beta}) + \rho_f u_\alpha u_\beta u_\gamma \quad (27)$$

with the transport coefficients equal to

$$D = c_{s,g}^2\left(\tfrac{1}{\omega_g}-\tfrac{1}{2}\right)\Delta t,$$

$$\nu = c_{s,f}^2\left(\tfrac{1}{\omega_f}-\tfrac{1}{2}\right)\Delta t. \quad (28)$$

Adding first and second order equations gives

$$(S_1+\epsilon S_2)\rho_f = -K_\alpha\bar{j}_{f,\alpha},$$

$$(S_1+\epsilon S_2)\rho_g = -K_\alpha\bar{j}_{g,\alpha} + q,$$

$$(S_1+\epsilon S_2)\bar{j}_{f,\alpha} = -K_\beta\Pi_{\alpha\beta} + F_\alpha \quad (29)$$

with the fluxes equal to

$$\bar{j}_{f,\alpha} = \rho_f\bar{u}_\alpha,$$

$$\Pi_{\alpha\beta} = \rho_f c_{s,f}^2\delta_{\alpha\beta} + \rho_f\bar{u}_\alpha\bar{u}_\beta - \rho_f\nu(\partial_\alpha\bar{u}_\beta + \partial_\beta\bar{u}_\alpha),$$

$$\bar{j}_{g,\alpha} = \rho_g\bar{u}_\alpha - D\partial_\alpha\rho_g. \quad (30)$$

By replacing the operators with derivatives, $\epsilon S_1+\epsilon^2 S_2=\partial_t$ and $\epsilon K_\alpha=\partial_\alpha$, we obtain the required continuity equation, momentum, and energy balance equation, as set in Eq. (3).

Hence via the inverse Chapman-Enskog expansion we have shown that the lattice BGK scheme is consistent with (i) convection diffusion if MB constraints are satisfied up to

TABLE I. Velocity set of the D2Q9 lattice.

i	$c_{i,x}$	$c_{i,y}$
0	0	0
1	$+c_1$	0
2	0	$+c_2$
3	$-c_1$	0
4	0	$-c_2$
5	$+c_1$	$+c_2$
6	$-c_1$	$+c_2$
7	$-c_1$	$-c_2$
8	$+c_1$	$-c_2$

second order, and (ii) fluid dynamics if MB constraints are satisfied up to *third* order. Below we have summarized the MB constraints formulated for $|f^{eq}\rangle$ up to third order:

$$\langle 1|f^{eq}\rangle = \rho,$$

$$\langle c_\alpha|f^{eq}\rangle = \rho u_\alpha,$$

$$\langle c_\alpha c_\beta|f^{eq}\rangle = \rho c_s^2 \delta_{\alpha\beta} + \rho u_\alpha u_\beta,$$

$$\langle c_\alpha c_\beta c_\gamma|f^{eq}\rangle = \rho c_s^2 (u_\alpha \delta_{\beta\gamma} + u_\beta \delta_{\alpha\gamma} + u_\gamma \delta_{\alpha\beta}) \tag{31}$$

and the constraints for the source term and body force:

$$\langle 1|\mathcal{G}\rangle = q\Delta t; \quad \langle 1|\mathcal{F}\rangle = 0,$$

$$\langle c_\alpha|\mathcal{G}\rangle = 0; \quad \langle c_\alpha|\mathcal{F}\rangle = F_\alpha \Delta t,$$

$$;\langle c_\alpha c_\beta|\mathcal{F}\rangle = 0. \tag{32}$$

Note that above, we have not imposed any restriction on the lattice. However, the MB constraints set limits to the lattice symmetry. In the next section we will analyze the MB constraints for the rectangular D2Q9 lattice.

IV. RECTANGULAR AND SQUARE D2Q9 LATTICE

For implementing the lattice Boltzmann scheme on a particular type of lattice, the equilibrium distribution has to be constructed via linear combinations of eigenvectors of the collision operator. Here, we construct equilibrium distributions for convection diffusion and fluid flow LB schemes on rectangular D2Q9 lattices, for which the popular *square* D2Q9 lattice is a subset. The velocity set associated with the rectangular D2Q9 lattice is given in Table I below. Given are the Cartesian components of the particle velocities $c_{i,\alpha}$. Mind that in general $c_1 \neq c_2$. Because in the general case of rectangular lattices the collision operator is not symmetric, we have to consider both left (L) and right (R) eigenvectors [1]. In the following L and R eigenvectors will also be denoted in the Dirac notation as bra and ket vectors, respectively: $\langle v_n|$ and $|\tilde{v}_n\rangle$.

As mentioned above, the equilibrium distribution functions are constructed as linear combinations of the eigenvectors (with $0 \leq n \leq 8$):

$$|f^{eq}\rangle = \sum_n \frac{\langle v_n|f^{eq}\rangle}{N_n}|\tilde{v}_n\rangle,$$

$$|g^{eq}\rangle = \sum_n \frac{\langle v_n|g^{eq}\rangle}{N_n}|\tilde{v}_n\rangle. \tag{33}$$

Notice that the required factors $\langle v_n|f^{eq}\rangle$ follow from the MB constraints, and the norms are equal to $N_n = \langle v_n|\tilde{v}_n\rangle$.

Note that in lattice Boltzmann it is common practice to truncate $|f^{eq}\rangle$ at $\mathcal{O}(u^2)$, or in other words the moments $\langle v_n|f^{eq}\rangle = 0$ for $v_n = \mathcal{O}(c^3)$ and higher order. Hence in the case of D2Q9 lattices we truncate $|f^{eq}\rangle$ at $n=5$.

We proceed with construction of the eigenvectors. The lower order eigenvectors are fully determined by the collision invariants ρ_f, ρ_g, and $\rho_f u_\alpha$, and are denoted as $\langle v_0| = \langle 1|$, $\langle v_1| = \langle c_x|$, $\langle v_2| = \langle c_y|$. For the higher order eigenvectors there is still some freedom in their definition. A natural choice for the eigenvectors are the tensor Hermite polynomials [19]. They have the elegant property that the components of the right eigenvector $\tilde{v}_{n,i}$ are equal to the component of the left eigenvector times a weight factor: $\tilde{v}_{n,i} = w_i v_{n,i}$. The weight factors w_i appear in the global equilibrium distributions $f_i(\mathbf{u}=0) = w_{f,i}\rho_f$ and $g_i(\mathbf{u}=0) = w_{g,i}\rho_g$. As such, their values are determined by the MB constraints. As the rectangular D2Q9 lattice has inversion symmetry, all odd moments of the weight factors are zero. Consequently, the remaining constraints on the weight factors are

$$\langle 1|w\rangle = 1; \quad \langle c_\alpha c_\beta|w\rangle = c_s^2. \tag{34}$$

These constraints do not fully determine the weight factors, rendering an extra degree of freedom: c_T^2. We define the weight factors as

$$w_0 = 1 - 2w_1 - 2w_2 - 4w_5,$$

$$w_1 = w_3 = \frac{c_s^2}{2c_1^2} - 2w_5,$$

$$w_2 = w_4 = \frac{c_s^2}{2c_2^2} - 2w_5,$$

$$w_5 = w_6 = w_7 = w_8 = \frac{c_s^2 c_T^2}{4c_1^2 c_2^2}. \tag{35}$$

Physical realizability says that all weights are positive and less than unity [7], and thus set limits to c_s^2, c_T^2, or the aspect ratio c_1/c_2. Though realizability is neither necessary nor sufficient for numerical stability, it is generally thought to help stability [7,20]. Instability is thought to be caused by nonpositivity of the particle distribution function f_i [6,7,20]. In entropic lattice Boltzmann schemes [7] positivity of f_i is guaranteed via the H theorem. However, these entropic schemes are lacking the mathematical and computational simplicity of regular LB schemes, and are thus rarely used.

TABLE II. Set of L eigenvectors of the D2Q9 lattice.

n	$\langle v_n\|$	N_n
0	$\langle 1\|$	1
1	$\langle c_x\|$	c_s^2
2	$\langle c_y\|$	c_s^2
3	$\langle c_x c_y\|$	c_s^4
4	$\langle c_x^2-c_s^2\|$	$(c_1^2-c_s^2)c_s^2$
5	$\langle c_y^2-c_s^2\|$	$(c_2^2-c_s^2)c_s^2$
6	$\langle c_x(c_y^2-c_s^2)\|$	N_6
7	$\langle c_y(c_x^2-c_s^2)\|$	N_7
8	$\cdots$	N_8

Further, we note that above the weight factors are given in general form. The weight factors for $|f^{(0)}\rangle$ and $|g^{(0)}\rangle$ need not be identical, and can thus have different values for the free parameters: $c_{s,f}^2$, $c_{s,g}^2$, $c_{T,f}^2=c_\nu^2$ and $c_{T,g}^2$.

Below we will show that isotropy of the viscosity sets further constraints on these free parameters. One of these isotropy constraints, $c_s^2=c_T^2$, makes the set of eigenvectors equal to the natural basis of tensor Hermite polynomials. In the following we assume $c_s^2=c_T^2$ for both $|f\rangle$ and $|g\rangle$. For convection diffusion there are more possible choices of the set of eigenvectors [21]. It happens that for a particular choice of eigenvectors, and in the case of $\omega_g=1$, the lattice Boltzmann scheme is *identical* to the classical Lax-Wendroff scheme [4]. The Lax-Wendroff scheme is a second order accurate finite volume scheme, based on central differencing, and a modified explicit time integration [22].

Via Gramm-Schmidt orthogonalization we obtain the full set of eigenvectors, which are listed together with the norms $N_n=\langle v_n|\tilde{v}_n\rangle$ in Table II. For $n>5$, the norms are not specified as they are not required for constructing $|f^{eq}\rangle$.

For part of the analysis in the following sections it is convenient to define an alternative basis with $\langle v_4'|=\langle v_4|+\langle v_5|=\langle c_x^2+c_y^2-2c_s^2|$ and $\langle v_5'|=\langle v_4|-\langle v_5|=\langle c_x^2-c_y^2|$.

Knowing the eigenvectors for $n\leq 5$, we can construct the equilibrium distribution function. Using the spectral decomposition and the MB constraints, we obtain

$$f_i^{eq}=w_i\rho\left(1+\frac{c_{i,\alpha}u_\alpha}{c_s^2}+\frac{(c_{i,x}^2-c_s^2)u_x^2}{c_s^2(c_1^2-c_s^2)}+\frac{(c_{i,y}^2-c_s^2)u_y^2}{c_s^2(c_2^2-c_s^2)}+\frac{c_{i,x}c_{i,y}u_xu_y}{c_s^4}\right). \tag{36}$$

Observe from Table II that we have only two independent eigenvectors of $O(c^3)$, that is because $|c_\alpha^3\rangle\sim|c_\alpha\rangle$. Consequently it is in general not possible to satisfy the constraint for $\Gamma_{\alpha\alpha\alpha}=3c_s^2j_\alpha$, except for the special case of a *square* lattice with $c_s^2=c^2/3$. In that case the third order moment is $\Gamma_{\alpha\alpha\alpha}=c_\alpha^2j_\alpha=3c_s^2j_\alpha$.

Below, we will show that in the regime of weakly compressible flow the MB constraints can also be satisfied for the rectangular lattice.

Weakly compressible regime

In the regime of weakly compressible flow, for which holds $K_\alpha j_\alpha=0$, one needs the traceless (dissipative) momentum tensor to follow Newton's law [6]:

$$\tilde{\Pi}_{\alpha\beta}^{(1)}=\Pi_{\alpha\beta}^{(1)}-\tfrac{1}{2}\,\mathrm{tr}[\Pi_{\alpha\beta}^{(1)}]. \tag{37}$$

Using $K_\alpha j_\alpha=0$, we have $S_1\Pi_{\alpha\beta}^{(0)}=c_s^2K_\alpha j_\alpha=0$, and consequently

$$\tilde{\Pi}_{\alpha\beta}^{(1)}=-\left(\tfrac{1}{\omega_f}-\tfrac{1}{2}\right)K_\gamma\tilde{\Gamma}_{\alpha\beta\gamma}. \tag{38}$$

From Table II we compute $\Gamma_{xxy}=\langle c_x^2c_y|wc_y\rangle=c_\nu^2j_y$, and $\Gamma_{xyy}=\langle c_y^2c_x|wc_x\rangle=c_\nu^2j_x$, and consequently the off-diagonal elements of the dissipative momentum flux are

$$\tilde{\Pi}_{xy}^{(1)}=-\left(\tfrac{1}{\omega_f}-\tfrac{1}{2}\right)(K_x\Gamma_{xxy}+K_y\Gamma_{xyy})=-\left(\tfrac{1}{\omega_f}-\tfrac{1}{2}\right)c_\nu^2(K_xj_y+K_yj_x). \tag{39}$$

Using $\Gamma_{xxx}=c_1^2j_x$, $\Gamma_{yyy}=c_2^2j_y$, we compute the trace of dissipative momentum flux:

$$\mathrm{tr}[\Pi_{\alpha\beta}^{(1)}]=-\left(\tfrac{1}{\omega_f}-\tfrac{1}{2}\right)[(c_1^2-c_\nu^2)K_xj_x+(c_2^2-c_\nu^2)K_yj_y]. \tag{40}$$

Note that $\mathrm{tr}[\Pi_{\alpha\beta}^{(1)}]=\langle c_x^2+c_y^2-2c_s^2|f^{(1)}\rangle$ is the projection of the first-order perturbation onto the eigenvector $\langle v_4'|=\langle c_x^2+c_y^2-2c_s^2|$. The relaxation of this (projected) perturbation is via the effective viscosity $\nu_{eff}=\frac{1}{2}\nu+\zeta$, where ζ is the bulk viscosity, which has no physical meaning in the weakly compressible regime. Numerically speaking, the effective viscosity will be related to the damping of (undesired) sound waves. For the rectangular grid the effective viscosity will be anisotropic, but this will have no significant effect on the flow in the weakly compressible regime. If sound waves are still significant, one can increase the effective viscosity via choosing another eigenvalue for the energy eigenvector [thereby creating a multiple relaxation time (MRT) scheme, cf. [23]].

The diagonal components of the traceless momentum tensor become:

$$\begin{aligned}\tilde{\Pi}_{xx}^{(1)}&=-\left(\tfrac{1}{\omega_f}-\tfrac{1}{2}\right)\left[\tfrac{1}{2}(c_1^2-c_\nu^2)K_xj_x-\tfrac{1}{2}(c_2^2-c_\nu^2)K_yj_y\right]\\&=-\left(\tfrac{1}{\omega_f}-\tfrac{1}{2}\right)\left[\tfrac{1}{2}(c_1^2+c_2^2)-c_\nu^2\right]K_xj_x,\\ \tilde{\Pi}_{yy}^{(1)}&=-\left(\tfrac{1}{\omega_f}-\tfrac{1}{2}\right)\left[\tfrac{1}{2}(c_2^2-c_\nu^2)K_yj_y-\tfrac{1}{2}(c_1^2-c_\nu^2)K_xj_x\right]\\&=-\left(\tfrac{1}{\omega_f}-\tfrac{1}{2}\right)\left[\tfrac{1}{2}(c_1^2+c_2^2)-c_\nu^2\right]K_yj_y.\end{aligned} \tag{41}$$

In the last lines of the above equalities, we have used again $K_\alpha j_\alpha=0$. Note that the diagonal elements of the traceless momentum flux is equal to the projection $\tilde{\Pi}_{\alpha\alpha}^{(1)}=\frac{1}{2}\langle c_x^2-c_y^2|f^{(1)}\rangle$. For consistency with Navier-Stokes flow (with isotropic viscosity) in the weakly compressible regime, it is required that

$$\tilde{\Pi}_{\alpha\alpha}^{(1)}=\nu K_\alpha j_\alpha \tag{42}$$

which is satisfied if

$$c_\nu^2 = c_{s,f}^2 = \frac{c_1^2 + c_2^2}{6}. \tag{43}$$

Note that this condition is consistent with the above derived condition for satisfying the MB constraints on the *square* lattice (without the weakly compressible flow assumption), namely $c_s^2 = c^2/3$. We have also obtained the relation for the (shear) viscosity:

$$\nu = c_\nu^2 \left(1/\omega_f - \tfrac{1}{2}\right)\Delta t. \tag{44}$$

This finding is consistent with the results of van Coevorden *et al.* [19], who have found that for the two shear eigenmodes the linearized lattice Boltzmann equation holds:

$$\nu_1 = \nu = \langle c_x c_y | \Omega_f^{-1} - \tfrac{1}{2} | w c_x c_y \rangle / N_2,$$

$$\nu_2 = \nu = \langle c_x^2 - c_y^2 | \Omega_f^{-1} - \tfrac{1}{2} | w (c_x^2 - c_y^2) \rangle / N_2. \tag{45}$$

Analogously, the general expression for the diffusivity (tensor) is

$$D_{\alpha\beta} = \langle c_\alpha | \Omega_g^{-1} - \tfrac{1}{2} | w c_\beta \rangle \tag{46}$$

which indicates ways to implement anisotropy in the diffusivity, namely via the eigenvalues of $\Omega_g^{-1} - \frac{1}{2}$, related to eigenvector $\langle c_\beta |$ and the norms $\langle c_\alpha | w c_\beta \rangle$.

First order perturbations in weakly compressible regime

Below, we give leading order approximations for $|f^{(1)}\rangle$ and $|g^{(1)}\rangle$ which are very useful for formulating initial and boundary conditions.

As the equilibrium distribution, we apply spectral decomposition to the first order perturbations:

$$|g^{(1)}\rangle = \sum_n \frac{\langle v_n | g^{(1)} \rangle}{N_n} |\tilde{v}_n\rangle,$$

$$|f^{(1)}\rangle = \sum_n \frac{\langle v_n | f^{(1)} \rangle}{N_n} |\tilde{v}_n\rangle. \tag{47}$$

Note that conservation of mass, momentum, and energy imply $\langle v_n | g^{(1)} \rangle = 0$ for $n = 0$, and $\langle v_n | f^{(1)} \rangle = 0$ for $n < 3$. Furthermore, the definition of the dissipative heat and momentum flux Eq. (26), state the values of the nonzero moments at leading order. Upon subsequent application of Fourier and Newton flux laws, Eq. (26), the expressions for the transport coefficients, Eq. (28), and the moments of the source terms Eq. (25) we obtain

$$|g^{(1)}\rangle \approx -\frac{\Delta t}{\omega_g} \partial_\alpha \rho_g | w c_\alpha \rangle,$$

$$|f^{(1)}\rangle \approx -\frac{\Delta t}{\omega_f} \rho_f (\partial_\alpha \bar{u}_\beta + \partial_\beta \bar{u}_\alpha) | w (c_\alpha c_\beta - c_{s,f}^2 \delta_{\alpha\beta}) \rangle. \tag{48}$$

Hence the nonequilibrium distributions $|g^{(1)}\rangle$ and $|f^{(1)}\rangle$ are (to leading order) proportional to the gradient in the conserved quantities ρ_g and u_α, as required by the flux laws.

V. THIRD ORDER CHAPMAN-ENSKOG EXPANSION

In the above *inverse* Chapman-Enskog expansion, up to *second* order, we have shown that the LB schemes are consistent with convection diffusion and Navier-Stokes flow. The LB schemes still contain degrees of freedom, i.e., ω_g, ω_f, and $c_{s,g}^2$, by which one can increase the accuracy and stability. Ways to do that follow from the extension of the Chapman-Enskog expansion to *third* order, as argued in our Introduction and Appendix A.

Before starting the third order Chapman-Enskog analysis we first point out that detailed analysis of a MRT-LB scheme for convection diffusion [21] shows that it is required that $\omega_{g,1} = \omega_{g,3}$. This condition is naturally satisfied by the lattice BGK scheme, and consequently the third order Chapman-Enskog expansion is presented only for case of the lattice BGK scheme.

We start with the equations in the hierarchy of third order in ϵ:

$$-\omega_g |g^{(3)}\rangle = D_1 |g^{(2)}\rangle + \left[S_2 + \tfrac{1}{2} D_1^2\right] |g^{(1)}\rangle + \left[S_3 + S_2 D_1 + \tfrac{1}{6} D_1^3\right] \times |g^{(0)}\rangle,$$

$$-\omega_f |f^{(3)}\rangle = D_1 |f^{(2)}\rangle + \left[S_2 + \tfrac{1}{2} D_1^2\right] |f^{(1)}\rangle + \left[S_3 + S_2 D_1 + \tfrac{1}{6} D_1^3\right] \times |f^{(0)}\rangle. \tag{49}$$

We proceed with taking the moments of the above equations, making use of $\langle 1 | g^{(n)} \rangle = 0$, $\langle 1 | f^{(n)} \rangle = 0$, $\langle c_\alpha | f^{(n)} \rangle = 0$ for $n > 0$, and $\langle 1 | D_1 | g^{(0)} \rangle = 0$, $\langle 1 | D_1 | f^{(0)} \rangle = 0$:

$$-S_3 \rho_g = \langle 1 | D_1 | g^{(2)} \rangle + \tfrac{1}{2} \langle 1 | D_1^2 | g^{(1)} \rangle + \tfrac{1}{6} \langle 1 | D_1^3 | g^{(0)} \rangle,$$

$$-S_3 \rho_f = \langle 1 | D_1 | f^{(2)} \rangle + \tfrac{1}{2} \langle 1 | D_1^2 | f^{(1)} \rangle + \tfrac{1}{6} \langle 1 | D_1^3 | f^{(0)} \rangle,$$

$$-S_3 j_{f,\alpha} = \langle c_\alpha | D_1 | f^{(2)} \rangle + \tfrac{1}{2} \langle c_\alpha | D_1^2 | f^{(1)} \rangle + \tfrac{1}{6} \langle c_\alpha | D_1^3 | f^{(0)} \rangle. \tag{50}$$

Next, we express the perturbations in terms of $|f^{(2)}\rangle$ and $|f^{(0)}\rangle$ in first order perturbation $|f^{(1)}\rangle$ using the hierarchy of equations:

$$\langle 1 | D_1^3 | g^{(0)} \rangle = -\omega_g \langle 1 | D_1^2 | g^{(1)} \rangle,$$

$$\langle 1 | D_1 | g^{(2)} \rangle = -\left(\frac{1}{\omega_g} - \frac{1}{2}\right) \langle 1 | D_1^2 | g^{(1)} \rangle,$$

$$\langle 1 | D_1^3 | f^{(0)} \rangle = -\omega_f \langle 1 | D_1^2 | f^{(1)} \rangle,$$

$$\langle 1 | D_1 | f^{(2)} \rangle = 0,$$

$$\langle c_\alpha | D_1^3 | f^{(0)} \rangle = \left(1 - \tfrac{1}{2}\omega_f\right) \langle c_\alpha | D_1^2 | f^{(1)} \rangle,$$

$$\langle c_\alpha | D_1 | f^{(2)} \rangle = -\left(\frac{1}{\omega_f} - \frac{1}{2}\right) K_\beta \langle c_\alpha c_\beta | f^{(1)} \rangle \tag{51}$$

and insert it in the above equations:

$$-S_3 \rho_g = -\omega_g \left[\left(\frac{1}{\omega_g} - \frac{1}{2}\right)^2 - \frac{1}{12}\right] \langle 1 | D_1^2 | g^{(1)} \rangle = \left[\left(\frac{1}{\omega_g} - \frac{1}{2}\right)^2 - \frac{1}{12}\right] \langle 1 | D_1^3 | g^{(0)} \rangle,$$

$$-S_3\rho_f = \left(\tfrac{1}{2}-\tfrac{\omega_f}{6}\right)\langle 1|D_1^2|f^{(1)}\rangle = \left(\tfrac{1}{2}-\tfrac{\omega_f}{6}\right)\left(\tfrac{1}{\omega_f}-\tfrac{1}{2}\right)K_\alpha K_\beta \Pi^{(1)}_{\alpha\beta},$$

$$-S_3 j_{f,\alpha} = -\omega_f\left[\left(\tfrac{1}{\omega_f}-\tfrac{1}{2}\right)^2-\tfrac{1}{12}\right]\langle c_\alpha|D_1^2|f^{(1)}\rangle = \left[\left(\tfrac{1}{\omega_f}-\tfrac{1}{2}\right)^2-\tfrac{1}{12}\right]\langle c_\alpha|D_1^3|f^{(0)}\rangle. \quad (52)$$

It must be noted that the above equations for ρ_f and $j_{f,\alpha}$ have already been shown by Qian and Chen [13], but they have not drawn any conclusions with respect to convergency or accuracy of the LB scheme.

With respect to convergency, we note that $S_n\rho_g$ scales with Δx^n (at least up to third order $n=3$), and consequently we can conclude that lattice Boltzmann schemes will converge with decreasing lattice spacing.

Accuracy and stability of the LB schemes can be improved if all right-hand sides of the above equations vanish, rendering $S_3\rho_g=0$, $S_3\rho_f=0$, and $S_3 j_{f,\alpha}=0$. In consecutive order we analyze the required conditions.

$S_3\rho_g=0$ holds if the *third* order MB constraint is satisfied,

$$\langle \tilde{c}^3|g^{(0)}\rangle = 0, \quad (53)$$

or if the relaxation parameter satisfies

$$\left(\frac{1}{\omega_g}-\frac{1}{2}\right)^2 = \frac{1}{12}. \quad (54)$$

For the D2Q9 lattice the third order MB constraint for $|g^{(0)}\rangle$ can only be satisfied on a *square* lattice for $c_s^2=c^2/3$. On a rectangular D2Q9 lattice, the third order moment cannot be satisfied for any value of c_s^2, even in the limit of weakly compressible flow, as for convection diffusion in general $K_\alpha\rho_g u_\alpha \neq 0$. Hence for *rectangular* lattice $S_3\rho_g=0$ can only be obtained for the special value of the relaxation parameter, as follows from Eq. (54): $\omega_g=3-\sqrt{3}$. By fixing ω_g one does *not* fix the diffusion coefficient as $c_{s,g}^2$ is a free parameter.

The condition $S_3\rho_f=0$ cannot be met with any value of the relaxation parameter. However, it is zero in the limit of *weakly compressible* flow, for it holds:

$$K_\alpha K_\beta \Pi^{(1)}_{\alpha\beta} = K_\alpha K_\beta (K_\alpha j_\beta + K_\beta j_\alpha) = 2K_\alpha^3 j_\alpha = 0. \quad (55)$$

$S_3 j_{f,\alpha}=0$ holds if the *fourth* order MB constraint is satisfied:

$$\langle \tilde{c}^4|f^{(0)}\rangle = 0 \quad (56)$$

or if the relaxation parameter satisfies:

$$\left(\frac{1}{\omega_f}-\frac{1}{2}\right)^2 = \frac{1}{12}. \quad (57)$$

For any D2Q9 lattice the fourth order MB constraint cannot be satisfied, and hence $S_3 j_{f,\alpha}=0$ can only be obtained by the special value of $\omega_f=3-\sqrt{3}$. However, this fixes the kinematic viscosity to one single value, as the third order MB constraints require $c_{s,f}^2=(c_1^2+c_2^2)/6$.

We conclude with a note that in literature there is some debate on the convergency of the Chapman-Enskog expansion of the classical Boltzmann equation [24,25]. From third order analysis follows that the dispersion coefficient of acoustic modes with sufficiently short wavelengths are positive, instead of negative—meaning that the acoustic waves are not damped but amplified. This is an artifact of the Chapman-Enskog analysis—but does not show in reality. Hence it is questioned whether results from higher order Chapman-Enskog are a good approximation of generalized hydrodynamics occurring at moderate and high Knudsen numbers.

Above we have used the Chapman-Enskog analysis as a numerical tool for investigating consistency, convergency, and accuracy. As stated in Appendix A, there is a high degree of equivalence with von Neuman stability analysis—a common tool in numerical analysis of traditional numerical schemes like finite difference and finite volume. Hence we can safely assume that Chapman-Enskog analysis is also a valid tool for numerical analysis.

However, the divergence of higher order Chapman-Enskog analysis indicates that one must be careful with conclusions of Chapman-Enskog analysis for hydrodynamics. Also the equivalence between Chapman-Enskog analysis and perturbation analysis hints in this direction. Results of perturbation analysis are in principle only valid for linear schemes (such as convection diffusion)—as it is based on Laplace transforms. Application to hydrodynamics requires linearization of the lattice Boltzmann scheme, but still these approximate results are considered useful [26]. Nonlinearity divergence of kinetic or acoustic modes with short wavelengths can be coupled back to longer wavelengths. Hence due to nonlinearity results obtained with higher order Chapman-Enskog analysis might not hold true and should be carefully checked numerically.

Below we will analyze only the convection-diffusion scheme for third order accuracy, because the third order hydrodynamics scheme has limited nondegrees of freedom. For the *linear* convection diffusion scheme, we still expect that the above derived theoretical results hold true.

VI. GAUSSIAN DENSITY PROFILE IN UNIFORM FLOW FIELD

By means of the well-known benchmark problem of a Gaussian density profile in a uniform flow field **u** we investigate the performance of the convection-diffusion scheme—without a direct coupling to a (time evolving) flow field. The flow field in this problem is uniform in space, and constant in time, and is at an angle with the Cartesian axes. In this analysis we investigate the properties of the scheme particularly with respect to numerical diffusion, dispersion, and cross-wind diffusion; problems which typically arise at high grid Peclet numbers, defined as $\mathrm{Pe}_\alpha^*=u_\alpha\Delta x_\alpha/D$ [22].

At first we compare the performance of several classes of the lattice Boltzmann schemes, namely (i) the Lax-Wendroff type of scheme ($\omega_g=1.0$), which we also have denoted as the finite lattice Boltzmann scheme (FLB) [4], (ii) the lattice BGK scheme (with $c_{s,g}^2=c^2/3$), (iii) a general lattice Boltzmann scheme (with $c_{s,g}^2<c^2/3$, and $\omega_g>1$), and (iv) the optimal lattice Boltzmann scheme (OPT), with $\omega_g=3-\sqrt{3}$.

This first comparison is performed on a square grid, with $\mathrm{Pe}_x^*=100$, $\mathrm{Pe}_y^*=0$, $\mathrm{Cr}_x=0.05$, $\sigma_0^2=9$. The initial values of the

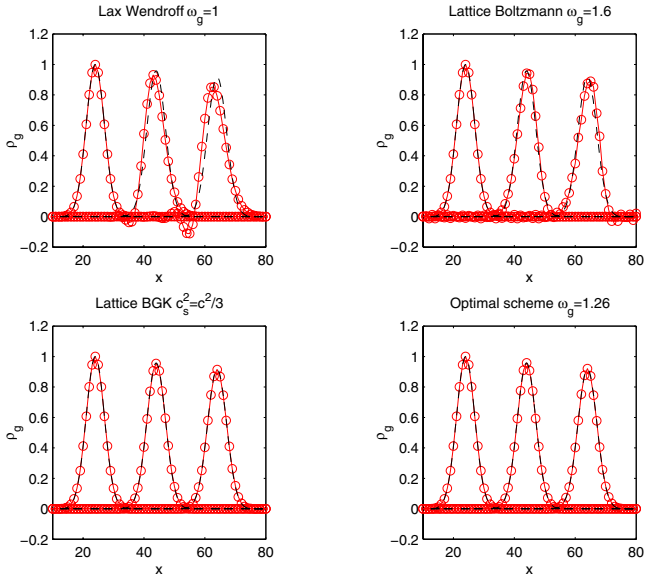

FIG. 1. (Color online) Gaussian profile in uniform flow field on a square grid, according to (a) Lax-Wendroff type of scheme, (b) a general lattice Boltzmann scheme, (c) lattice BGK scheme with $c_s^2=c^2/3$, and (d) optimal scheme with $\omega_g=3-\sqrt{3}=1.26$.

particle distribution functions are set equal to

$$g_i(\mathbf{x},0) = g_i^{eq}(\rho_g(\mathbf{x},0),\mathbf{u}) + g_i^{(1)}[\nabla\rho_g(\mathbf{x},0)] \tag{58}$$

with the initial density profile equal to

$$\rho_g(\mathbf{x},0) = \exp\left(-\frac{(\mathbf{x}-\mathbf{x}_0)^2}{2\sigma_0^2}\right). \tag{59}$$

Here $\mathbf{x}_0$ is the initial position of the maximum of the Gaussian profile, and σ_0 is a measure of its initial width. From the above given initial profile, the gradient $\nabla\rho_g(\mathbf{x},0)$ is computed and inserted in Eq. (48), to obtain the first order perturbation $g_i^{(1)}$.

Profiles are shown in Fig. 1 for times $t_e/\Delta t=0$, 400, 800, and are compared to analytical solution. As one can observe, the Lax-Wendroff scheme and the general lattice Boltzmann scheme are showing numerical oscillations, but the lattice BGK scheme and the optimal scheme are virtually free of numerical oscillations *and* numerical diffusion. Hence the Lax-Wendroff type of scheme and the general lattice Boltzmann scheme show behavior typical of second order accurate schemes. The general lattice Boltzmann scheme is even showing instability in the range of $1.7<\omega_g<1.99$ [similar to the convection diffusion scheme on a (rectangular) D2Q5 lattice [2]]. The little numerical dispersion and numerical diffusion of the lattice BGK scheme and the optimal scheme are expected results, as for these schemes $S_3\rho_g=0$, in which case the Chapman-Enskog analysis predicts improved accuracy and stability. Compared to the Lax-Wendroff scheme or the general lattice Boltzmann scheme (with $c_{s,g}^2\neq c^2/3$) we have indeed observed a wider stability range: the lattice BGK and the optimal scheme are stable for larger grid Peclet numbers with any $1\geq\omega_g<2$.

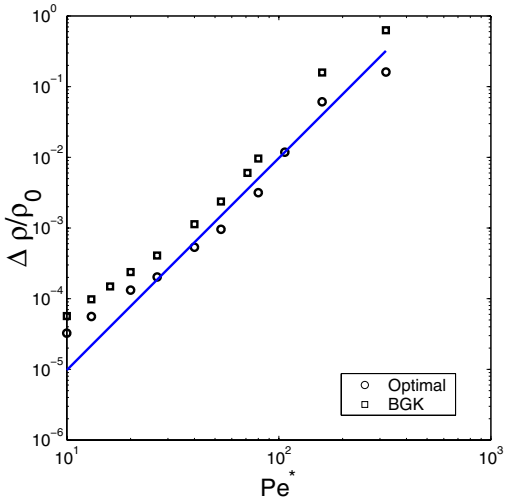

FIG. 2. (Color online) Relative numerical error $\Delta\rho/\rho_0$ in maximal density as a function of grid Peclet number Pe^*, for optimal and BGK schemes.

Little numerical diffusion and numerical dispersion are typical of third order accurate schemes. We investigate numerically whether the lattice BGK and optimal schemes are indeed third order accurate schemes via investigation of the numerical error as a function of the resolution $\sigma/\Delta x$. Simulations are performed with Peclet number $\mathrm{Pe}_L=uL_x/D=2560$, with L_x the system size. The number of grid points is taken from the range $8\leq L_x/\Delta x\leq 256$, and the number of time steps is taken equal for all simulations, such that Cr_x scales with the number of grid points $L_x/\Delta x$. We have chosen $\mathrm{Cr}_x=0.05$ in the case of $L_x/\Delta x=256$. The width of the Gaussian profile is chosen such that $L_x/\sigma_0=16$. The relative numerical error $\Delta\rho/\rho_0$ is determined of the maximal density value, after propagation over the distance $\frac{1}{2}L_x$ in uniform velocity field, with $u_y=0$. In Fig. 2 we have plotted the numerical error as a function of the grid Peclet number Pe_x^*, which scales with the size of the lattice spacing Δx. Here we observe that for high grid Peclet numbers the numerical error scales with Δx^3. However, for low grid Peclet numbers the numerical error scales with Δx^2. This second order behavior at low grid Peclet numbers can be attributed to the fact that in this regime the gradients are high, i.e., $\max(\Delta x\partial_x\rho_g/\rho_g)=\Delta x/\sigma_0=\epsilon>0.1$. Consequently, the errors induced by higher order modes are *not* negligible, and we observe deviation from the theoretical results of the Chapman-Enskog analysis, which is only valid for small values of ϵ.

Because of their better performance, only the lattice BGK and optimal schemes will be analyzed in the following. A more detailed analysis is obtained via computing the moments of the Gaussian profile. Below we list their definition and the values according to the analytical solution of the benchmark problem,

$$M_0 = \sum_n \rho_g(\mathbf{x}_n),$$

$$M_{1,\alpha} = \sum_n x_{n,\alpha}\rho_g(\mathbf{x}_n),$$

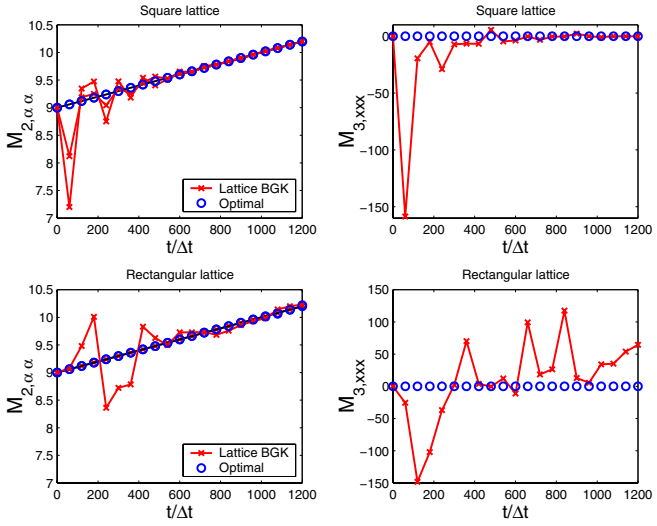

FIG. 3. (Color online) Second and third order moment of the Gaussian density profile on (a) square and (b) rectangular lattice for $\mathrm{Pe}_x=100$, obtained from the numerical solutions of the lattice BGK and optimal schemes. The solid line indicates analytical solution for the second order moment. The third order moment should be zero.

$$M_{2,\alpha\beta} = \sum_n (x_{n,\alpha} - \bar{x}_\alpha)(x_{n,\beta} - \bar{x}_\beta)\rho_g(\mathbf{x}_n),$$

$$M_{3,\alpha\beta\gamma} = \sum_n (x_{n,\alpha} - \bar{x}_\alpha)(x_{n,\beta} - \bar{x}_\beta)(x_{n,\gamma} - \bar{x}_\gamma)\rho_g(\mathbf{x}_n),$$

$$\frac{M_{1,\alpha}}{M_0} = \bar{x}_\alpha(t) = x_{0,\alpha} + u_\alpha t,$$

$$\frac{M_{2,\alpha\beta}}{M_0} = \sigma^2_{\alpha\beta}(t) = (\sigma_0^2 + 2Dt)\,\delta_{\alpha\beta},$$

$$\frac{M_{3,\alpha\beta\gamma}}{M_0} = 0. \tag{60}$$

We have analyzed the moments for the case of a square grid, $\mathrm{Cr}_x=0.05$, $\mathrm{Cr}_y=0.025$, $\mathrm{Pe}_x=100$, $\mathrm{Pe}_y=50$, and $\sigma_0^2=9$. In Fig. 3 we have plotted σ_{xx}^2, σ_{yy}^2, and $M_{3,xxx}/M_0$. The first order moments $M_{1,\alpha}$ follow the analytical solution very accurately, and therefore they are not shown. From the figure we observe there are differences in performance between lattice BGK and the optimal schemes. In the initial phase the moments of the lattice BGK are showing numerical oscillations, but which damp out. After this initial phase the moments follow the theoretical values. The moments of the optimal scheme follow quite closely the theoretical values for all times. The numerical oscillations exhibited by the lattice BGK scheme are excited by the improper initial conditions. Because $\omega_g \approx 2$ in the case of the lattice BGK scheme, the numerical oscillations (hard kinetic modes) are poorly damped. In the case of the optimal scheme $\omega_g=1.26$, leading to strong damping of the hard kinetic modes. We have found similar behavior for diffusion [1], where we have shown via eigenmode analysis that hard kinetic modes are poorly damped if ω_g approaches 2.

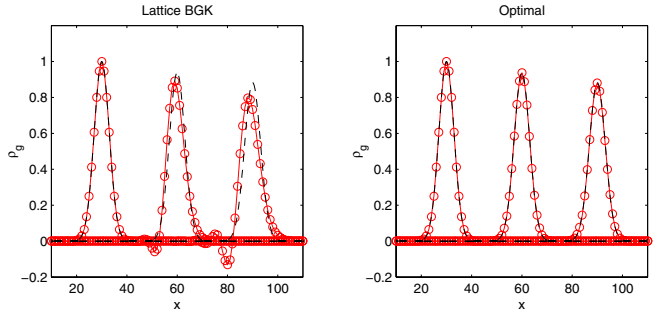

FIG. 4. (Color online) Gaussian profile in uniform flow field on a rectangular grid, according to (a) lattice BGK scheme with $c_s^2=(c_1^2+c_2^2)/6$, and (b) optimal scheme with $\omega_g=3-\sqrt{3}=1.26$.

We proceed the analysis of the benchmark problem for rectangular grids, and with a uniform velocity field at an angle with the Cartesian axes. We analyze only the lattice BGK scheme with $c_{s,g}^2=(c_1^2+c_2^2)/6$ and the optimal scheme with $\omega_g=3-\sqrt{3}$.

Note that the lattice BGK scheme is restricted to a limited range of the aspect ratio of the grid, due to the physical requirement of positivity of the weight factors: $w_i>0$. Having defined $c_{T,g}^2=c_{s,g}^2=(c_1^2+c_2^2)/6$, it follows from Eq. (35) that $0.45<c_1/c_2<2.2$. For the optimal scheme positivity of the weight factors can always be assured by a suitable choice of $c_{s,g}^2$, taken from the range $0<c_{s,g}^2<\min\{c_1^2,c_2^2\}$.

Simulations are performed for $c_1/c_2=0.5$, $\mathrm{Cr}_x=0.05$, and $\mathrm{Cr}_y=0.025$, $\mathrm{Pe}_x^*=100$, $\mathrm{Pe}_y^*=25$. We have computed the moments, which are also plotted in Fig. 3. We observe that the moments obtained from the optimal scheme again follow closely the theoretical values. The moments obtained from the lattice BGK scheme show again numerical oscillations, albeit that the third order moment is not damped—but grows unbounded due to numerical dispersion. Cross sections of the density profiles at times $t/\Delta t=600$, 1200 are shown in Fig. 4, where the numerical oscillations in the solution of the lattice BGK scheme are clearly shown.

As indicated by its moments, the solution of the optimal scheme on the rectangular grid is free of any numerical dispersion and numerical diffusion. The diffusion is isotropic, as both σ_{xx}^2, σ_{yy}^2 are practically equal, and follow the theoretical values very accurately. Hence the optimal scheme does not exhibit crosswind diffusion (also indicated by $M_{2,xy}\approx 0$)—even if the velocity field is at an angle with the lattice axes.

At aspect ratios $c_1/c_2>2$ or $c_1/c_2<0.5$ the lattice BGK scheme is unstable, as expected from the negativity of the weight factors. To show that the optimal scheme is stable at higher aspect ratios, we have performed simulations at $c_1/c_2=3$, $\mathrm{Pe}_x^*=40$, $\mathrm{Cr}_x=0.05$, and $\mathrm{Cr}_y=0.03$. In Figs. 5 and 6 we show the simulation results: a contour plot of the density profile—showing that the diffusion stays isotropic, and a collapse plot of cross sections through the center of the density profile at times $t\Delta t=0$, 600, 1200—showing that the optimal scheme accurately follows the analytical solution.

Summarizing, on the rectangular grid both the lattice BGK scheme and the optimal scheme perform as predicted

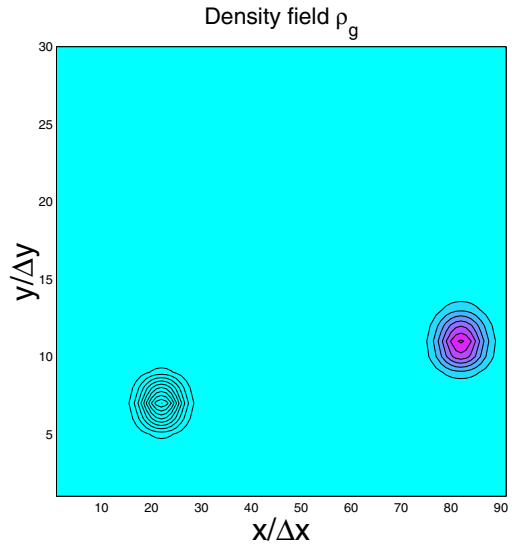

FIG. 5. (Color online) Contour plot of density field ρ_g with Gaussian profile in uniform flow field on a rectangular grid, with aspect ratio $c_1/c_2=3$ with numerical solution at times $t=0$ and $t\Delta t=1200$.

by the Chapman-Enskog expansion. The lattice BGK scheme is second order accurate (showing numerical dispersion like the Lax-Wendroff scheme), and the optimal scheme is even third order accurate (in the regime of high grid Peclet numbers only), showing practically no numerical diffusion or dispersion.

VII. DIFFERENTIALLY HEATED CAVITY

With the well-known benchmark problem of natural convection in a square cavity [27], we further test the above developed LB schemes. In this problem convection diffusion and fluid flow are coupled via the buoyancy body force in the Navier-Stokes equation. The buoyancy is linear with the fluids density, which is assumed to be slightly linear dependent on temperature T (Boussinesq approximation). The governing (steady state) equations are

$$\partial_\alpha(\rho u_\alpha T) = \alpha \partial_\alpha^2 T,$$

$$\partial_\alpha(\rho u_\alpha u_\beta) = -\partial_\beta p + \nu \partial_\alpha^2 \rho u_\beta + \beta \rho g_\beta (T - T_{ref}). \quad (61)$$

Here T is the fluid temperature, α is the thermal diffusivity, β is the thermal expansion coefficient, g_β is the gravitational acceleration, and T_{ref} is a defined reference temperature. The dimension of the square cavity is L. At the walls of the cavity no slip boundary conditions are applied for the fluid flow, and for the energy transport the top and bottom walls are adiabatic, and the left and right walls are isothermal at different temperatures $T_h > T_c$. The natural convection problem is governed by two dimensionless numbers: the Prandtl number $\mathrm{Pr}=\nu/\alpha$, and the Rayleigh number $\mathrm{Ra}=g\beta\Delta(T_h - T_c)L^3/\nu\alpha$. The transport of energy from the hot to the cold wall is characterized by the Nusselt number at the wall (located at $x=0$): $\mathrm{Nu}=L\partial_\alpha T(x=0)/(T_h - T_c)$.

In the lattice Boltzmann model the no-slip and adiabatic boundary conditions are implemented via bounce back conditions. Isothermal boundary conditions are implemented, cf. Ref. [15]. Nu is computed via determining the heat flux at the isothermal walls, as stated in Appendix C. The total number of iterations for solving is taken equal to $N_{steps}=10^4\mathrm{Fo}^*$, with the grid Fourier number $\mathrm{Fo}^*=\alpha\Delta x/\Delta x^2$. As an initial condition, we take a vertically stratified temperature field if $\mathrm{Ra}<10^4$, and horizontally stratified otherwise.

The first series of simulations is performed on the square grid, to compare the various schemes. We have distinguished the following schemes:

(i) FLB/FLB (with $\omega_f=\omega_g=1.00$);
(ii) OPT/OPT (with $\omega_f=\omega_g=1.26$);
(iii) BGK/BGK No. 1 (with $\omega_f=\omega_g=1.50$);
(iv) BGK/BGK No. 2 (with $\omega_f=\omega_g=1.90$);
(v) BGK/OPT (with $\omega_f=1.90$ and $\omega_g=1.26$).

We have taken the Prandtl number of air, namely $\mathrm{Pr}=0.71$, as in Ref. [27]. The Rayleigh number is varied between $10^2 < \mathrm{Ra} < 10^7$, for a lattice size of $L/\Delta x=64$. If $\mathrm{Ra} > 2\times 10^8$ there is no time independent solution, due to bifurcation of the natural convection.

In Fig. 7 we have plotted Nu vs Ra and have compared that with the results of de Vahl Davis, which scales as $\mathrm{Nu} \sim \mathrm{Ra}^{0.33}$. We observe that at low Ra numbers all schemes produce practically the same result as the benchmark solution of de Vahl Davis. Hence we can conclude that all schemes are consistent with the equations governing natural convection.

The poorest performance is by the FLB/FLB scheme, as expected. The accuracy of the schemes increases with increasing ω_f. The solution of the LB schemes starts to deviate if $\mathrm{Cr}_y=u_{y,max}\Delta t/\Delta y > 0.1$, thus when compressibility errors become important. As an example, in Table III we have listed the values of $\mathrm{Cr}_y=u_{y,max}\Delta t/\Delta y$ and Fo^* for the various schemes at $\mathrm{Ra}=10^5$. At this Rayleigh number the FLB/FLB and OPT/OPT schemes are unstable, while the other schemes are stable because $\mathrm{Cr}_y < 0.1$ even while the grid Peclet num-

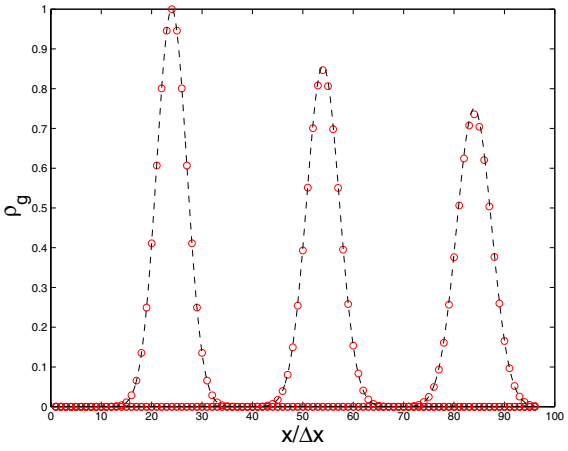

FIG. 6. (Color online) Collapse plot of Gaussian profile in uniform flow field on a rectangular grid, with aspect ratio $c_1/c_2=3$ at times $t/\Delta t=0$, 600, 1200—according to the optimal scheme (symbols) and analytical solution (lines).

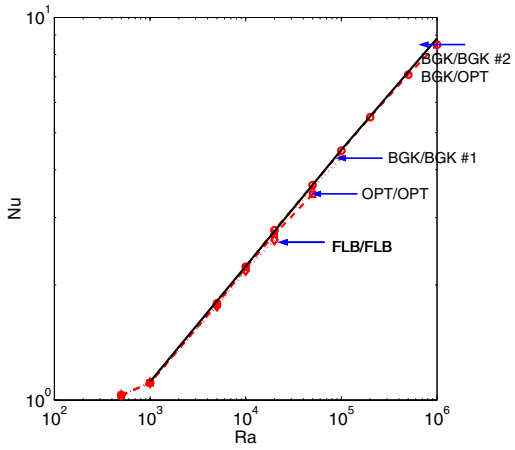

FIG. 7. (Color online) Nusselt number Nu vs the Rayleigh number Ra, according to various LB schemes (symbols) and the benchmark solution of de Vahl Davis (solid line). Simulations are performed on a square lattice of size 64 Δx. Arrows indicate where the different schemes deviate from the benchmark solution—where beyond they become unstable.

ber exceeds 2: $\mathrm{Pe}^*_{y,max}=\mathrm{Cr}_y/\mathrm{Fo}^*>2$. The performance of the BGK/BGK No. 2 and BGK/OPT scheme is more or less identical, indicating that the accuracy is merely determined by ω_f (or Cr_y). At $\mathrm{Ra}=10^7$ the solution of the BGK/BGK No. 2 and BGK/OPT schemes is still stable, but quite inaccurate and fluctuating between Nu=13 and Nu=14, because of the poor resolution of the boundary layer.

After checking the consistency of the schemes with natural convection, we investigate our hypothesis that the mass fluxes are really defined on the boundary of the lattice cells. We have computed the velocity field using both formulations, Eqs. (B7) and (22). For $\mathrm{Ra}=10^4$ we have plotted the contours of the u_x and u_y field, as calculated with both definitions of the mass flux. From Fig. 8 one can conclude that both ways of computing the velocities are consistent with each other. We have also drawn the same conclusion for $\mathrm{Ra}=10^5$, for which we have plotted the velocity profile midway in the square cavity, and compared it to the values given in the benchmark solution. In Fig. 9 the line plots of u_x and u_y are given, and both calculation methods produce the same results and are consistent with the maximal value of the benchmark solution.

From the line plot of the velocities at $\mathrm{Ra}=10^5$, we clearly see a thin boundary layer forming along the vertical walls, while the isotherm near the horizontal walls get stratified.

Rectangular grid

The consistency of the scheme on the rectangular grid has been checked by the correlation Nu(Ra). The BGK/BGK No. 2 scheme has been shown to be unstable for any Ra, whereas the BGK/OPT scheme reproduced similar results as on the square grid, and therefore these results are not presented. Consequently we have focused on the accuracy of the scheme for $\mathrm{Ra}=10^7$. The aspect ratio is taken $c_1/c_2=2$. We have computed the order of accuracy by comparing Nu with the benchmark value $\mathrm{Nu}_\infty=16.53$. For that we have varied the resolution in the range $2.5\times10^{-3}\leq\Delta x/L\leq5.0\times10^{-3}$. Results are shown in Fig. 10. With linear regression we have analyzed that the error $(\mathrm{Nu}-\mathrm{Nu}_\infty)$ is a quadratic function of the resolution $\Delta x/L$, and thus the BGK/OPT scheme on the rectangular lattice is second order accurate, as predicted by the inverse Chapman-Enskog expansion.

The contour plot of the temperature in Fig. 10 is very similar to the one displayed by LeQuere [28], who has listed the benchmark results for $\mathrm{Ra}=10^7$. We repeat here again that the BGK scheme for fluid flow is restricted to aspect ratios of $0.5\leq c_1/c_2\leq2.0$, and thus also holds for the BGK/OPT scheme solving for natural convection.

TABLE III. Courant and grid Fourier numbers at $\mathrm{Ra}=10^5$.

	BGK No. 2	BGK No. 1	OPT	FLB
ω_f	1.9	1.5	1.26	1
Cr_y	0.013	0.084	0.148	0.252
Fo^*	0.012	0.078	0.138	0.235

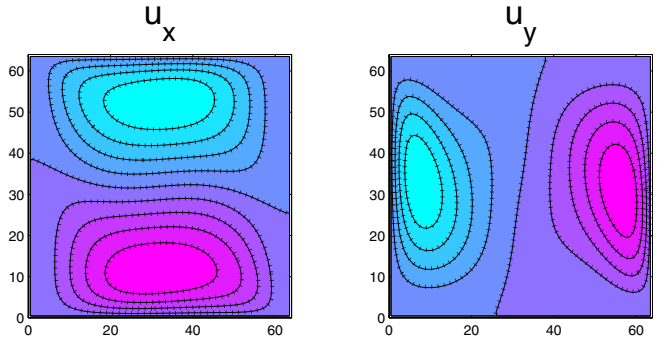

FIG. 8. (Color online) Contour plot of horizontal (u_x) and vertical velocity (u_y) for $\mathrm{Ra}=10^4$. Solid contour lines are velocities computed at centers of lattice cells, and dotted lines are velocities computed at boundaries of lattice cells. Contours are practically identical to that of de Vahl Davis [27].

VIII. VOLUMETRIC HEATING

Here we consider natural convection with a nonuniform source term. As said, the objective of this short case study is

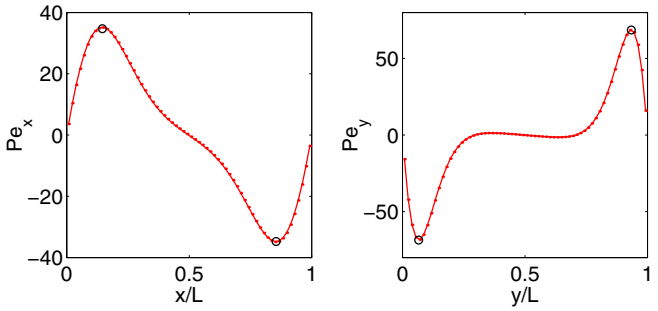

FIG. 9. (Color online) Line plot of midplane horizontal (u_x) and vertical velocity (u_y) for $\mathrm{Ra}=10^5$. Solid lines are velocities at boundaries of lattice cells, and dots are interpolated from velocities obtained at centers of lattice cells. Black circles are the benchmark values of de Vahl Davis [27].

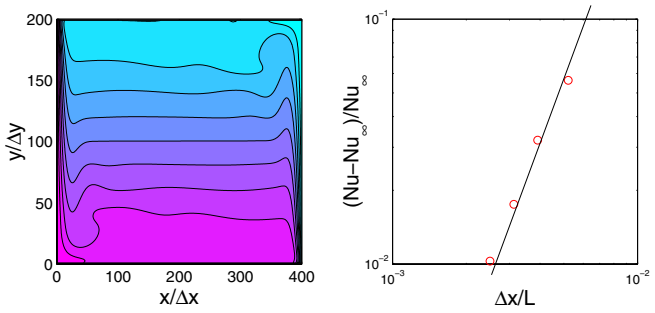

FIG. 10. (Color online) (a) Contour plot of temperature at Ra $=10^7$, and (b) relative error in Nusselt number as a function of resolution $\Delta x/L$—showing second order convergency.

to investigate the findings with respect to the heat flux, in the case of a source term in the convection diffusion equation. We assume that the fluid is contained in a square cavity with isothermal walls, with $T_{wall}=0$, and the volumetric heating following Lambert's law:

$$Q(x) = Q_0\{\exp(-\lambda_Q x) + \exp[-\lambda_Q(L-x)]\}. \quad (62)$$

Simulations are performed on a rectangular lattice of $L/\Delta x = 30$ and $L/\Delta y = 40$, with $\lambda_Q/L = 0.3$. The temperature plot is shown in Fig. 11 at the left. We observe natural convection, with two distinct hot spots, slightly above the horizontal midplane and at $x/L \approx 1/4$ and $x/L \approx 3/4$. In case of more or less uniform volumetric heating one would expect a single hotspot at $x/L=1/2$—but due to strong nonuniform heating at the center at $x/L=1/2$ there is little volumetric heating and there is a strong cooling effect of the downward convective heat flux. Hence we expect that natural convection due to nonuniform heating has rich physics.

In Fig. 11 at the right we have plotted the (decomposed) heat flux at the vertical midplane $(x/L=1/2)$. The dashed line indicates the total heat flux $j_{g,\alpha}(x+\frac{1}{2}\Delta x_\alpha)$, located at the boundary of the Wigner-Seitz cells—as computed with Eq. (C1). Using the mass fluxes $j_{f,\alpha}(x+\frac{1}{2}\Delta x_\alpha)=\rho_f u_\alpha$ and the (interpolated) temperatures $\rho_g(x+\frac{1}{2}\Delta x_\alpha)$ we have computed the convective heat flux (dotted line):

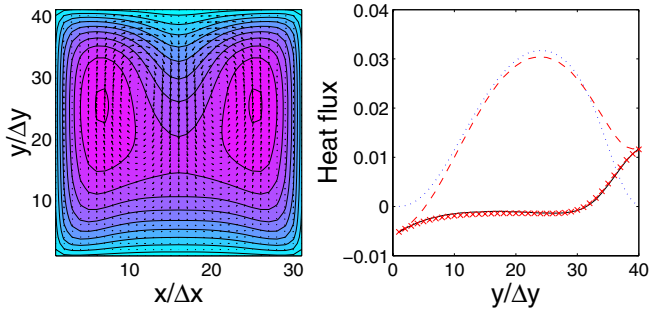

FIG. 11. (Color online) Simulation results of natural convection due to nonuniform volumetric heating, with (a) contour plot of temperature, and (b) heat flux at vertical midplane with details explained in the main text.

$$j^{(0)}_{g,\alpha}\left(x+\tfrac{1}{2}\Delta x_\alpha\right) = (\rho_g u)\left(x+\tfrac{1}{2}\Delta x_\alpha\right) \quad (63)$$

and the dissipative part of the heat flux (solid line):

$$j^{(1)}_{g,\alpha}\left(x+\tfrac{1}{2}\Delta x_\alpha\right) = j_{g,\alpha}\left(x+\tfrac{1}{2}\Delta x_\alpha\right) - j^{(0)}_{g,\alpha}\left(x+\tfrac{1}{2}\Delta x_\alpha\right). \quad (64)$$

The dissipative heat flux $j^{(1)}_{g,\alpha}$ is compared with the finite difference approximation of Fourier's law:

$$j^{(1)}_{g,\alpha}\left(x+\tfrac{1}{2}\Delta x_\alpha\right) \approx -D[\rho_g(x+\Delta x_\alpha)-\rho_g(x)]/\Delta x_\alpha \quad (65)$$

which is displayed with symbols. From the figure we observe that the definition of the dissipative heat halfway on the lattice nodes $j^{(1)}_{g,\alpha}(x+\frac{1}{2}\Delta x_\alpha)$ is consistent with the finite difference approximation. Hence we conclude that also in the general case of natural convection with a volumetric heat source, the heat flux is correctly calculated at the boundaries of the Wigner-Seitz cells, similar to the mass flux.

IX. CONCLUSIONS

Via inverse Chapman-Enskog analysis we have shown that for the lattice Boltzmann schemes to be consistent with convection diffusion and fluid flow, the moments of the equilibrium distribution should equal those of the Maxwell-Boltzmann distribution (the so-called MB constraints), as has been noted earlier by McNamara and Alder [6]. For fluid flow the MB-constraints up to third order have to be satisfied, while for convection diffusion the MB constraints up to *second* order have to be satisfied. In both cases the MB constraints render a Galilean invariant scheme with second order accuracy. Next to the MB constraints, there is also the constraint of isotropic transport coefficients-as expressed by van Coevorden [19]. These constraints set the required lattice symmetry. It follows that the constraints can be satisfied on the rectangular D2Q9 grid, if one assumes fluid flow to be weakly compressible.

Accuracy of the LB scheme can be increased if (i) *higher* order MB constraints are satisfied, or (ii) relaxation parameters (i.e., eigenvalues of collision operator) are set equal to *magic* numbers, which follow from (quite tedious) *higher* order Chapman-Enskog analysis. Higher order MB constraints can be satisfied on the rectangular grid for convection diffusion only. If the relaxation parameter equals the "magic" number $\omega=3-\sqrt{3}$, then the convection-diffusion scheme has also third order accuracy, yet only at moderate gradients $(\epsilon<0.1)$. Also this magic number holds for fluid flow, albeit that one fixates the viscosity thus limiting the LB scheme to the (near-)Stokes flow regime.

The parallel analysis of fluid flow and convection-diffusion scheme with source terms has shown us that (i) fluxes should be defined on the boundaries of the Wigner-Seitz cells, surrounding the lattice sites, and consequently (ii) the equilibrium distribution need *not* be modified for including the source terms in the scheme, contrary to many other recent studies on body forces in fluid flow schemes, cf. Refs. [11,12]. The source terms can be implemented simply by adding an extra term, for which the constraints of its velocity moments follow from the inverse Chapman-Enskog analysis.

Numerical solutions (on both square and rectangular lattices) of well-known benchmark problems for convection

diffusion and natural convection have confirmed that our theoretical findings are correct indeed. The performance of lattice Boltzmann for convection diffusion is quite remarkable; the standard lattice BGK scheme has third order accuracy (on the square grid) and is even quite accurate for problems with high grid Peclet numbers ($\mathrm{Pe}^* \sim 1000$), provided that gradients are not that steep. The performance of the optimal scheme (with the relaxation parameter equal to the magic number $\omega_g = 3-\sqrt{3}$) is even better than for the lattice BGK scheme: though it also has third order accuracy, it shows significantly fewer numerical oscillations induced by the initial values $g_i(\mathbf{x},0)$. In the literature this good performance of lattice Boltzmann for convection diffusion is often not recognized [29–31]; there is really no need to resort to hybrid schemes, where LB is combined with particle tracking or finite difference schemes for solving convection diffusion.

The performance of the lattice Boltzmann scheme for fluid flow on a rectangular grid is limited to a small range of aspect ratios, namely $0.5 \leq c_1/c_2 \leq 2$. Outside this range some weight factors w_i become negative, leading to instability. This finding confirms the earlier notion in literature [7,20] that negativity of the weight factors can be a cause for instability.

For developing LB schemes on irregular grids our analysis shows that for Galilean invariant fluid flow schemes with isotropic viscosity, one requires either lattices with multiple speeds also to next-neighboring lattice sites (in order to satisfy the MB constraints), or possibly multiple relaxation time (MRT) schemes with eigenvalues of the collision operators equal to some magic number to compensate for numerical errors. From a physical point of view the last option is not quite attractive, while from a computational point of view the first option is not very attractive. We anticipate, if one relaxes the constraints on Galilean invariance and isotropy, that second order accurate LB schemes on structured curvilinear irregular D2Q9 grids are possible—provided that the lattice spacing varies gradually (also demanded by the stability constraints), and consequently, the errors due to anisotropy or Galilean invariance are of order Δx^3.

ACKNOWLEDGMENTS

The author thanks Irina Ginzburg and Dominiq d'Humieres for valuable discussions, and Matthieu Ernst for help with the third order Chapman-Enskog expansion.

APPENDIX A: EQUIVALENCE OF PERTURBATION ANALYSIS AND CHAPMAN-ENSKOG

In this Appendix we show that there is equivalence of perturbation analysis and Chapman-Enskog analysis of the convection-diffusion LB scheme. From this equivalence the arguments for the introduction of the multitime scale expansion of the Chapman-Enskog analysis follow naturally. We begin with the introduction of the perturbation analysis, from which we obtain a hierarchy of equations. Subsequently, this hierarchy is compared to that of the Chapman-Enskog analysis. We conclude with the note on the relation with the perturbation analysis and the von Neumann stability analysis, a standard tool in numerical analysis.

Perturbation analysis is based on the ansatz that the Fourier mode is a solution of the Lattice Boltzmann equation. The ansatz is taken because the Fourier mode with wave vector $\mathbf{k}$,

$$\rho_g(\mathbf{x},t) = \tilde{\rho}_g(\mathbf{k},s)\exp(ik_\alpha x_\alpha + st), \tag{A1}$$

is a solution of the convection diffusion equation:

$$\partial_t \rho_g + \partial_\alpha \rho_g u_\alpha = D\partial_\alpha^2 \rho_g. \tag{A2}$$

From substitution of the Fourier mode in the convection diffusion equation follows the dispersion relation:

$$s(\mathbf{k}) = -ik_\alpha u_\alpha - Dk^2. \tag{A3}$$

The Fourier mode of the LB scheme is similar to Eq. (A1):

$$g_i(\mathbf{x},t) = \tilde{g}_i(\mathbf{k},s)\exp(ik_\alpha x_\alpha + st). \tag{A4}$$

Its dispersion relation is yet unknown, but for consistency it must follow the same as for convection diffusion, i.e., Eq. (A3). The Fourier mode is a perturbation of the global equilibrium distribution $\tilde{g}_i^{(0)}(\tilde{\rho}_g = \tilde{\rho}_{g,0}, \mathbf{u}=0)$, with uniform density $\rho_{g,0}$ and zero velocity.

Substitution of the ansatz in the lattice Boltzmann equation leads to the following eigenvalue problem:

$$[\exp(ik_\alpha \Delta x_{i,\alpha} + s\Delta t) - 1]\tilde{g}_i(\mathbf{k},s) = \omega_g[\tilde{g}_i(\mathbf{k},s) - \tilde{g}_i^{(0)}], \tag{A5}$$

where we have inserted $\tilde{g}_i^{(0)}$ as the equilibrium distribution.

Generally this eigenvalue problem must be solved numerically [1]. An approximate analytical expression for the dispersion relation can be obtained by a perturbation analysis.

In the perturbation analysis the eigenmode $\tilde{g}_i(\mathbf{k},s)$ and the relaxation rate $s(\mathbf{k})$ are expanded as polynomials of the wave number k:

$$\tilde{g}_i(k,s) = \tilde{g}_i^{(0)} + (ik)\tilde{g}_i^{(1)} + (ik)^2\tilde{g}_i^{(2)} + O(k^3) \tag{A6}$$

$$s(\mathbf{k})\Delta t = (ik)s_1 + (ik)^2 s_2 + O(k^3). \tag{A7}$$

Furthermore, Taylor expansion is applied to $[\exp(ik_\alpha \Delta x_{i,\alpha} + s\Delta t) - 1]$. Substitution of the expansions render the following hierarchy of equations:

$$\begin{aligned} -\omega_g|\tilde{g}^{(1)}\rangle &= D_1|\tilde{g}^{(0)}\rangle, \\ -\omega_g|\tilde{g}^{(2)}\rangle &= D_1|\tilde{g}^{(1)}\rangle + \left(S_2 + \tfrac{1}{2}D_1^2\right)|\tilde{g}^{(0)}\rangle \end{aligned} \tag{A8}$$

with $D_1 = (s_1\Delta t + ik_\alpha \Delta x_{i,\alpha})$, and $S_2 = s_2\Delta t$. Observe the equivalence with the hierarchy obtained with the Chapman-Enskog analysis, Eq. (10) (while ignoring the source terms). The hierarchies are identical, only the above equations are formulated in Fourier space and those of the Chapman-Enskog analysis in real space.

Hence the operators are also related via Fourier-Laplace transform. The Laplace transform of a spatial derivative of a

function is $\mathcal{L}(\partial_\alpha|g\rangle)=ik_\alpha|\tilde{g}\rangle$ and of the time derivative is $\mathcal{L}(\partial_t|g\rangle)=s(\mathbf{k})\tilde{g}$. As the dispersion coefficient $s(\mathbf{k})$ can be expanded, also the time derivative can be expanded—which is the multitime scale expansion of the Chapman-Enskog analysis. From the dispersion relation for convection diffusion follows that $iks_1=ik_\alpha u_\alpha$ or rather $\epsilon\partial_{t1}$ is related to the convective time scale, and that $(ik)^2s_2=(ik)^2D$ and $\epsilon^2\partial_{t2}$ are related to the slower diffusive time scale. Hence the dispersion relation $s(\mathbf{k})$ for convection diffusion, Eq. (A3), gives natural arguments for the multitime scale analysis.

Perturbation analysis is only valid for small numbers of the dimensionless wave number $k_\alpha\Delta x$. This condition implies that the Chapman-Enskog analysis is only valid for small gradients. This follows from the notion that the gradient of the Fourier mode and the wave number are related:

$$\epsilon \sim ik_\alpha\Delta x = \frac{\Delta x\partial_\alpha g_i(\mathbf{x},t)}{\tilde{g}_i(\mathbf{k},s)} \ll 1. \tag{A9}$$

Hence the parameter in the Chapman-Enskog expansion ϵ defines a ratio of length scales, namely the lattice spacing Δx and the length scale of density gradients (or wavelength of the perturbation).

We further note that Fourier mode analysis of the dispersion relation of the lattice Boltzmann equation is mathematically equivalent with the von Neumann stability analysis [1]. Hence as with the von Neumann stability analysis, the above perturbation analysis, and the Chapman-Enskog analysis one investigates the consistency and the stability of the lattice Boltzmann scheme.

Consistency with convection diffusion is achieved if we obtain $s(\mathbf{k})=-ik_\alpha u_\alpha-(ik_\alpha)^2D+O(k^3)$. Stability demands that $|s(k)|<1$, and hence it sets some limits on Courant number $|\mathrm{Cr}_\alpha|<1$ and grid Fourier number $\mathrm{Fo}^*_\alpha<1$, with $\mathrm{Cr}_\alpha=u_\alpha\Delta t/\Delta x_\alpha$ and $\mathrm{Fo}^*_\alpha=D\Delta t/\Delta x^2_\alpha$. Furthermore, numerical oscillations will occur if $\mathrm{Im}[s(\mathbf{k})+ik_\alpha u_\alpha+(ik_\alpha)^2D]\neq 0$. Hence by performing perturbation analysis or Chapman-Enskog analysis to third order we can investigate this condition to leading order. Thus the LB scheme will show numerical oscillations if $s_3\neq 0$.

A final note to be made is that perturbation analysis can only be applied to linear or linearized lattice Boltzmann schemes [26], while Chapman-Enskog analysis can be applied to nonlinear LB schemes, like the schemes modeling fluid flow.

APPENDIX B: LOCATION OF THE MASS FLUX

We investigate the proper definition of the mass flux using a quiescent fluid enclosed in a cavity with solid walls, subject to gravity. This problem can be treated as a one-dimensional problem, and we assume a D1Q3 lattice Boltzmann model. Because the velocity field is zero, we can assume $f_i^{eq}=w_i\rho_f$. The lattice BGK equation describing this system is

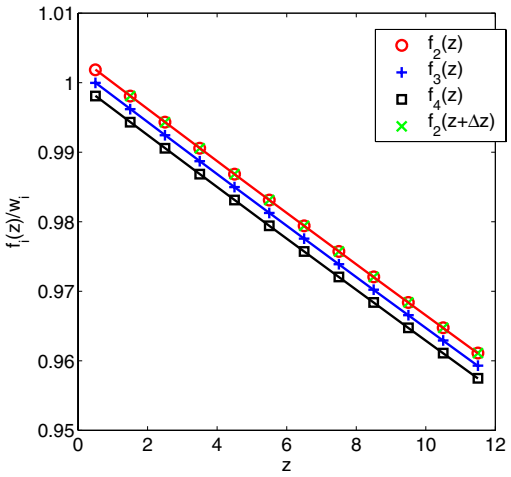

FIG. 12. (Color online) Comparison of numerical (symbols) and analytical (lines) steady state particle distributions of a lattice gas in a uniform gravity field.

$$f_i(z+\Delta z,t+\Delta t)-f_i(z,t)=-\omega_f[f_i(z,t)-f_i^{eq}(z,t)]+\mathcal{F}_i. \tag{B1}$$

We take the special case of $\omega_f=1$ and investigate the steady state solution. In steady state, the pressure profile is $p(z)=p_0-\rho_f gz$, with g the acceleration of the gravity field. As the lattice Boltzmann scheme uses the ideal gas equation of state, we have $\rho_f(z)c_s^2=p(z)$, with c_s^2 the speed of sound—which relates to the weight factors: $w_1=w_2=c_s^2/2c^2$. The forcing term is taken equal to

$$\mathcal{F}_i=-\rho_f g w_i c_i/c_s^2\Delta t. \tag{B2}$$

Observe that $\Sigma_i\mathcal{F}_ic_i=-\rho_f g\Delta t$, is the momentum transferred by the gravity field in time Δt. At internal nodes (at least one lattice spacing away from the wall), the steady state solution is (for $gc/c_s^2\ll 1$)

$$f_i(z)\approx w_i\rho_f(z)-\tfrac{1}{2}\mathcal{F}_i. \tag{B3}$$

The post collision distribution function is

$$f_i'(z)\approx w_i\rho_f(z)+\tfrac{1}{2}\mathcal{F}_i=w_i\rho_f(z+\Delta z_i)-\tfrac{1}{2}\mathcal{F}_i=f_i(z+\Delta z_i). \tag{B4}$$

At the bottom of the cavity $z=0$ we have a no flux boundary condition, which can be implemented with the well-known bounce back rule:

$$f_1\left(\tfrac{1}{2}\Delta z,t+\Delta t\right)=f_2'\left(\tfrac{1}{2}\Delta z,t\right)\approx w_2\rho_f\left(\tfrac{1}{2}\Delta z\right)-\tfrac{1}{2}\mathcal{F}_2+\mathcal{F}_2$$
$$=f_1\left(\tfrac{1}{2}\Delta z,t\right) \tag{B5}$$

with f_i' the post-collision particle distribution function. Hence the bounce back condition is consistent with the steady state solution.

Now we investigate the often used expression to compute the mass flux:

$$\tilde{j}_{f,z}(z) = [f_1(z) - f_2(z)]\Delta z/\Delta t \approx \mathcal{F}_1 \neq 0 \tag{B6}$$

which is in contradiction which the assumption of a quiescent fluid. The reason for this contradiction is because due to the forcing there is no momentum conservation (gravity adds momentum to the system) [15].

However, as advocated by van der Sman [2,15] and also recently by Capuani and co-workers [16], the mass flux must really be computed at the boundaries of the lattice cells, halfway along the lattice nodes:

$$j_{f,z}\left(z + \tfrac{1}{2}\Delta z\right) = [f_1(z + \Delta z) - f_2(z)]\Delta z/\Delta t = 0. \tag{B7}$$

Hence by measuring the velocity field at the lattice cell boundaries, the traditional intuitive scheme for implementing body forces can still be used.

We have checked our analysis with the numerical scheme used in Sec. VI, for describing the differentially heated cavity. We have initialized the cavity with uniform temperature, imposing a uniform buoyancy force. The density of the fluid is following $\rho_f(z+\Delta z)=\rho_f(z)(1+g\Delta z/c_s^2)$, and the particle distribution as follows Eq. (B3). The square lattice measures 12 by 12 cells, and the lattice BGK scheme is used with $\omega_f=1.5$ and $c_s^2=c^2/3$. After 10^4 iterations we collected the particle distribution and compared it to the theoretical prediction, Eq. (B3)—as shown in Fig. 12. Observe that $f_2(z)=f_4(z+\Delta z)$ and consequently the mass flux across the horizontal cell boundaries is zero, as required. Furthermore, in steady state the rest particles f_0 and the particles propagating horizontally only (f_1 and f_3) are invariant under collision.

APPENDIX C: LOCATION OF THE HEAT FLUX

For the convection-diffusion scheme we compute the flux $j_{g,\alpha}(\mathbf{x})$ at the interface between two adjacent Wigner-Seitz cells at $\mathbf{x}$ and $\mathbf{x}+\Delta\mathbf{x}_\alpha$. The flux is defined as

$$j_{g,\alpha}\left(\mathbf{x} + \tfrac{1}{2}\Delta x_\alpha, t\right) = \sum_{i'} c_{i,\alpha} g_i(\mathbf{x} + \Delta\mathbf{x}_i, t) + \sum_{i''} c_{i,\alpha} g_i(\mathbf{x}, t) \tag{C1}$$

with the ranges i' and i'' indicating the set of particles crossing the interface. As in the Chapman-Enskog analysis we split the particle distribution in an equilibrium and nonequilibrium part:

$$g_i(\mathbf{x},t) = g_i^{(0)}(\mathbf{x},t) + \epsilon g_i^{(1)}(\mathbf{x},t). \tag{C2}$$

For the equilibrium distribution we use

$$g_i^{(0)}(\mathbf{x},t) = \rho_g(\mathbf{x},t)|1\rangle + \frac{j_{g,\alpha}^{(0)}}{c_{s,g}^2}|c_\alpha\rangle \tag{C3}$$

and the nonequilibrium distribution:

$$g_i^{(1)}(\mathbf{x},t) = -\frac{\partial_\alpha \rho_g(\mathbf{x})}{\omega_g}|wc_\alpha\rangle - \frac{1}{\omega_g}|q^{(1)}\rangle. \tag{C4}$$

Inserting these equations into the flux definition, and performing Taylor expansion to $\rho_g(\mathbf{x}+\Delta\mathbf{x}_i,t)$ one obtains

$$j_{g,\alpha}\left(\mathbf{x} + \tfrac{1}{2}\Delta x_\alpha, t\right) - j_{g,\alpha}^{(0)}\left(\mathbf{x} + \tfrac{1}{2}\Delta x_\alpha, t\right) = -\left(\frac{1}{\omega_g} - \frac{1}{2}\right)c_{s,g}^2 \Delta t \partial_\alpha \rho_g\left(\mathbf{x} + \tfrac{1}{2}\Delta\mathbf{x}_\alpha, t\right). \tag{C5}$$

The heat flux at the interface can be decomposed in an equilibrium part: $j_{g,\alpha}^{(0)}=\rho_g(\mathbf{x}+\frac{1}{2}\Delta x_\alpha,t)u_\alpha(\mathbf{x}+\frac{1}{2}\Delta x_\alpha,t)$, and a nonequilibrium part $j_{g,\alpha}^{(1)}$ proportional to (i) the gradient in ρ_g *at* the interface and (ii) the thermal diffusivity $D=(1/\omega_g - \frac{1}{2})c_{s,g}^2\Delta t$. Observe that the terms originating from $g_i^{(1)}$, which are linear in $q^{(1)}$, cancel out. Furthermore, observe that the factor $\frac{1}{2}$ in the thermal diffusivity originates from the Taylor expansion of the leading term in the equilibrium distribution, while the term $\frac{1}{\omega_g}$ originates from the leading term in the nonequilibrium distribution.

[1] R. G. M. van der Sman and M. H. Ernst, J. Stat. Phys. **94**, 203 (1999).
[2] R. G. M. van der Sman and M. H. Ernst, J. Comput. Phys. **160**, 1 (2000).
[3] R. G. M. van der Sman, FGCS, Future Gener. Comput. Syst. **201**, 965 (2004).
[4] R. G. M. van der Sman, Comput. Fluids **35**, 849 (2006).
[5] J. M. V. A. Koelman, Europhys. Lett. **15**, 603 (1991).
[6] G. McNamara and B. Alder, Physica A **194**, 218 (1993).
[7] S. Succi, I. V. Karlin, and H. Chen, Rev. Mod. Phys. **74**, 1203 (2002).
[8] M. Bouzidi, D. d'Humieres, P. Lallemand, and L. S. Luo, J. Comput. Phys. **172**, 704 (2001).
[9] B. M. Boghosian and P. V. Coveney, Int. J. Mod. Phys. C **9**, 1231 (1998).
[10] R. Verberg and A. J. C. Ladd, J. Stat. Phys. **104**, 1191 (2001).
[11] J. M. Buick and C. A. Greated, Phys. Rev. E **61**, 5307 (2000).
[12] Z. Guo, C. Zheng, and B. Shi, Phys. Rev. E **65**, 046308 (2002).
[13] Y. H. Qian and S. Y. Chen, Phys. Rev. E **61**, 2712 (2000).
[14] E. G. Flekkoy, U. Oxaal, J. Feder, and T. Jossang, Phys. Rev. E **52**, 4952 (1995).
[15] R. G. M. van der Sman, Int. J. Mod. Phys. C **8**, 87 (1997).
[16] F. Capuani, I. Pagonabarraga, and D. Frenkel, J. Chem. Phys. **8**, 973 (2004).
[17] S. V. Patankar, *Numerical Heat Transfer and Fluid Flow* (Hemisphere, Washington, D.C., 1980).
[18] R. Herbin and O. Labergerie, Comput. Methods Appl. Mech. Eng. **147**, 85 (1997).
[19] D. V. van Coevorden, M. H. Ernst, R. Brito, and J. A. Somers, J. Stat. Phys. **74**, 1085 (1994).
[20] B. M. Boghosian *et al.*, Proc. R. Soc. London, Ser. A **457**, 717 (2001).
[21] R. G. M. van der Sman and M. H. Ernst (unpublished).
[22] Y. Wang and K. Hutter, Int. J. Numer. Methods Fluids **37**, 72 (2001).
[23] D. d'Humieres, I. Ginzburg, M. Krafczyk, P. Lallemand, and L. S. Luo, Philos. Trans. R. Soc. London, Ser. A **360**, 437

(2002).
[24] A. Santos, J. J. Brey, and J. W. Dufty, Phys. Rev. Lett. **56**, 1571 (1986).
[25] A. N. Gorban and I. V. Karlin, Phys. Rev. Lett. **77**, 282 (1996).
[26] P. Lallemand and L. S. Luo, Phys. Rev. E **61**, 6546 (2000).
[27] G. de Vahl Davis, Int. J. Numer. Methods Fluids **3**, 249 (1983).
[28] P. Le Quere, Comput. Fluids **20**, 29 (1991).
[29] R. M. H. Merks, A. G. Hoekstra, and P. M. A. Sloot, J. Comput. Phys. **183**, 563 (2002).
[30] A. Mezrhab, M. Bouzidi, and P. Lallemand, Comput. Fluids **33**, 623 (2004).
[31] J. A. Kaandorp, C. P. Lowe, D. Frenkel, and P. M. A. Sloot, Phys. Rev. Lett. **77**, 2328 (1996).